NASA

Technical Memorandum 84008

Aircraft and Satellite Measurement of Ocean Wave Directional Spectra Using Scanning-Beam Microwave Radars

Frederick C. Jackson, W. Travis Walton
Paul L. Baker

May 1982

National Aeronautics and
Space Administration

Goddard Space Flight Center
Greenbelt, Maryland 20771

AIRCRAFT AND SATELLITE MEASUREMENT OF OCEAN WAVE DIRECTIONAL SPECTRA USING SCANNING-BEAM MICROWAVE RADARS*

Frederick C. Jackson and W. Travis Walton

Laboratory for Atmospheric Sciences
NASA Goddard Space Flight Center, Greenbelt, Maryland 20771

Paul L. Baker

Computer Sciences Corporation, Silver Spring, Maryland 20910

May 1982

---

*To be published in <u>Wave Dynamics and Radio Probing of the Ocean Surface</u>, proceedings of a symposium, Miami, Florida, May 14-20, 1981, Plenum Press.

AIRCRAFT AND SATELLITE MEASUREMENT OF OCEAN WAVE DIRECTIONAL SPECTRA USING SCANNING-BEAM MICROWAVE RADARS

Frederick C. Jackson and W. Travis Walton

Laboratory for Atmospheric Sciences
NASA Goddard Space Flight Center, Greenbelt, Maryland 20771

Paul L. Baker

Computer Sciences Corporation, Silver Spring, Maryland 20910

ABSTRACT

A microwave radar technique for remotely measuring the vector wave number spectrum of the ocean surface is described. The technique, which employs short-pulse, noncoherent radars in a conical scan mode near vertical incidence, is shown to be suitable for both aircraft and satellite application. The technique has been validated at 10 km aircraft altitude, where we have found excellent agreement between buoy and radar-inferred absolute wave height spectra.

1. INTRODUCTION

For several years now, we have been endeavoring to develop a microwave radar technique for measuring ocean wave directional spectra that would be suitable for satellite application. Basically, we have been seeking to define an alternative to the coherent imaging radar approach that was adopted for Seasat, the nation's first oceanographic satellite (Beal et al., 1981). Our motivation has been to find an alternative measurement approach that would at the same time a) be simpler and less costly, b) be capable of truly global measurements, and c) be more accurate.

In this we believe we have been successful. Theoretically, and on the basis of aircraft flight experiments we have determined that such global-scale satellite measurements are feasible. The measurements can be made with relatively simple, noncoherent short-pulse radars operating in a conical scan mode near vertical incidence, $\theta \sim 10°$. No new technological developments are required. Rather, these measurements can be made with existing space-qualified hardware. For example, with some relatively minor modifications such as the addition of a modest-gain scanning antenna, the Seasat altimeter can be adapted to perform these measurements. The measurements are inherently of high resolution spectrally in both wave number and direction, and as we shall see, they will be remarkably accurate as well.

A typical satellite measurement geometry is illustrated in figure 1. For the assumed satellite altitude of 700 km and incidence angle of 10°, the radius of the scan pattern on the ocean surface is approximately 130 km. A 3-rpm antenna rotation rate is selected as a reasonable compromise between coverage and integration time requirements. The measurement cells (not to be confused with the instantaneous field of view, or antenna 'footprint') are roughly 130 km squares situated one on either side of the subsatellite track. Basically, the measurement product consists of two statistically stable estimates of the polar-symmetric vector wave number spectrum, one on either side of the subsatellite track. If less than 180° of look is allowed, then these measurements can be confined to an area considerably smaller than the nominal 130 km square as is evident from figure 1.

Although the technique we shall be considering employs short-pulse waveforms, it is not in its most fundamental aspect different from the two-frequency technique investigated theoretically by Alpers and Hasselmann (1978) and experimentally by Johnson et al. (1981). In both techniques the basic measurement principle is the same. This is the directional selectivity that results as a natural consequence of the phase-front matching of electromagnetic and ocean wave components. The choice of waveforms, and the manner of detection, is however a critical one. Jackson (1981)--hereinafter referred to as J--has shown that the narrowband two-frequency technique has, inherently, a very low signal-to-noise ratio (SNR) compared to the short-pulse technique. Basically, this is because the sea-spectrum is relatively broadband whereas the two-frequency beat-wave signal is comparatively narrowband. For large footprint dimensions this results in modulation signal power being detected only in a very narrow spectral band, and consequently, the signal energy is small compared to the fading variance.

Our work differs from that of Alpers and Hasselmann (1978) in another important respect. This is in the choice of incidence angles. Alpers and Hasselmann (1978) were concerned with large-angle measurements whereas our concern is with small angles of incidence. There are several reasons why we have chosen to study small-angle scatter. First, as should be apparent from the above discussion of the measurement geometry, small angles of incidence are necessary at satellite altitudes in order to keep the scan radius to a minimum. If the nadir angle is too large, the scan pattern on the surface may exceed the scale of homogeneity of the wave field. Second, the reflectivity modulation mechanism in near-vertical backscatter is simpler and more predictable than it is in large-angle backscatter. In the near-vertical, specular backscatter regime the contrast modulation does not depend on the strong--and essentially unpredictable--hydrodynamic modulation of the short Bragg-diffracting water wave. The modulation mechanism is primarily a geometrical tilting effect, and consequently, it is more amenable to accurate modelling. Another reason for choosing small incidence angles is an obvious one, that the greater cross-section and lower link loss near nadir demands less transmitter power and antenna gain. This is an important consideration in the wide-band measurement approach that we are advocating.

In the following we will discuss the three major conceptual elements that constitute the measurement technique, namely, 1) the principle of directional selectivity, 2) the modulation mechanism in near-vertical backscatter, and 3) the use of short-pulse waveforms to detect the range reflectivity modulation. The discussion is intended to provide a basic understanding of the measurement technique and to provide such results and formulas as will be found useful in the analysis of the aircraft data. For a fuller and more detailed theoretical treatment, the reader is referred to J.

2. THE MEASUREMENT TECHNIQUE

2.1 The principle of directional selectivity.

We are concerned with fairly narrow antenna beams in a high-altitude measurement geometry. The relevant geometry is illustrated in figure 1. The situation desired is one where a) the antenna footprint is large compared to the scale of the waves, and b) the curvature of the wavefront is small compared to the directional spread of the waves. Now obviously, if the lateral beam spot dimension is large compared to the scale of the waves, then the waves cannot be resolved in azimuth (short of resorting to synthetic aperture). Rather, the wave contrasts will be averaged laterally across the beam. What is the effect of this lateral averaging? To understand the effect, imagine a Fourier decomposition of the two-dimensional reflectivity field into an angular spectrum of plane contrast waves. (The reflectivity field can be imagined to be that measured by a very high resolution real-aperture imaging radar looking in the same azimuth direction.) Referring to figure 2, it is apparent that the effect of the lateral averaging is to eliminate or 'cancel out' any plane surface contrast wave that is not aligned with the beam direction. Only those surface waves whose phase fronts are 'matched' to the electromagnetic (em) phase front can survive the lateral averaging. The effect of the broad footprint is then to isolate, or resolve surface contrast wave components whose wave vectors $\underline{K} = (K, \phi)$ are aligned with the beam direction.

The directional resolution is determined by and limited by a) the finiteness of the beam spot size in azimuth L_y, and b) the curvature of the wave front within the beam spot. If we assume a Gaussian-shaped azimuth gain pattern,

$$G(y) = \exp(-y^2/2L_y^2) \tag{2.1}$$

then it follows (e.g., from the Fresnel zone solution in J) that the directional resolution $\delta\Phi$, defined as the half-power spectral window width in azimuth, is given by

$$\delta\Phi \sim \delta K_y/K = 2\sqrt{2\ln 2}\,[(KL_y)^{-2} + (L_y\cot\theta/2H)^2]^{1/2} \tag{2.2}$$

where H is the altitude. The first and second terms in (2.2) derive respectively from the finite-footprint and wave-front curvature effects. In our aricraft experiment geometry, $H \sim 10$ km, $\theta \sim 13°$, and $L_y \sim 300$ m. (half power width $L_y^* = 2\sqrt{2\ln 2}\, L_y \sim 700$ m). For a typical 200 m water wave, we have $\delta\Phi \sim 17°$. In a typical satellite measurement, $H = 700$ km, $\theta = 10°$, and $L_y = 8.5$ km ($L_y^* = 20$ km), in which case $\delta\Phi \sim 5°$.*

2.2 The reflectivity modulation in near-vertical backscatter.

Near vertical incidence, $\theta \lesssim 15°$, microwave backscatter from the sea occurs by means of quasi-specular reflections from wave facets

---

*The directional resolution quoted in J (equation 79) is wrong.

oriented normal to the radar's line of sight. The average backscatter cross-section σ^o is proportional to the probability density function (pdf) of orthogonal surface slopes satisfying the specular condition for backscatter: $\partial\zeta/\partial x = \tan\theta$; $\partial\zeta/\partial y = 0$. The cross-section is given by (e.g., Valenzuela, 1978):

$$\sigma^o(\theta,\Phi) = \rho\pi\sec^4\theta p(\tan\theta,0) \tag{2.3}$$

where p is the slope pdf expressed in the radar's coordinate system, x in the plane of incidence, and where ρ is a diffraction-modified normal incidence Fresnel reflectivity (Brown, 1978).

Hydrodynamic modulation is a second-order effect in near-vertical backscatter. Consider that, firstly, for most microwave frequencies, the most strongly forced waves, the gravity-capillary waves, lie under the diffraction limit (about three em wavelengths in the horizontal according to Brown (1978)). Thus, they are only weakly sensed, and to the extent that they are, it is via a diffuse diffraction field that can be only very weakly modulated by geometrical tilting. Secondly, the specular component derives from the entire wave ensemble, including waves on all scales, from the scale of the dominant waves we are seeking to measure down to the scale of the diffraction limit. For this large ensemble of waves, it is reasonable to assume that hydrodynamic forcing and wave-wave interaction effects are of secondary importance. To the extent that hydrodynamic nonlinearities effect the em modulation, they are to be attributed to the entire wave ensemble rather than a particular water wave component. Neglecting second-order effects, the surface can be treated as a free-wave superposition possessing Gaussian statistics. If the large-wave slopes are then assumed to be small compared to the total rms surface slope, the modulation can be modelled by the following linear 'tilt model'.

The backscatter cross-section of a small patch of sea surface of area A (cf. figure 3) is given by $\sigma = \sigma^o A$, where the normalized cross-section σ^o is assumed to be the average σ^o of the sea surface in a tilted reference frame. Thus, if θ' and Φ' are the local incidence and azimuth angles, we suppose that $\sigma^o(\text{patch}) = \sigma^o(\theta',\Phi')$. For small large-wave tilts δ, the fractional cross-section variation is given by

$$\frac{\delta\sigma}{\sigma} \simeq \frac{\delta\sigma^o}{\sigma^o} + \frac{\delta A}{A} \qquad (2.4)$$

The elementary surface area is that area contained in the range interval $c\Delta\tau/2$. To first order in δ, A is given by $A = \Delta y(c\Delta\tau/2)\csc\theta'$. Provided that $\delta << \theta$, the local incidence angle can be approximated by $\theta' \sim \theta - \partial\zeta/\partial x$. Thus, to first order in δ it follows that $\delta A/A = \cot\theta\ \partial\zeta/\partial x$. Since the azimuthal dependence of σ^o is small compared to the θ dependence, it follows that the tilt term $\delta\sigma^o/\sigma^o$ is also proportional to the large-wave slope component in the plane of incidence. From (2.3),

$$\frac{\delta\sigma^o}{\sigma^o} = -\frac{1}{p}\frac{\partial p}{\partial \tan\theta}\frac{\partial\zeta}{\partial x} + O(\delta^2) \qquad (2.5)$$

The fractional range-reflectivity modulation seen by the radar is $\delta\sigma/\sigma$ averaged laterally across the beam:

$$m(x,\Phi) = \frac{\int G^2(y)(\delta\sigma/\sigma)dy}{\int G^2(y)dy} \tag{2.6}$$

The directional modulation spectrum is defined by

$$P_m(K,\Phi) = (2\pi)^{-1}\int \langle m(x,\Phi)m(x+\xi,\Phi)\rangle \exp(-iK\xi)d\xi \tag{2.7}$$

where the angle brackets denote ensemble average. Now let G be given by the Gaussian pattern (2.1), and consider the limiting case of very large footprints, $KL_y \gg 1$. It is easy to show then that P_m is proportional to the directional slope spectrum as

$$P_m(K,\Phi) = \frac{\sqrt{2\pi}}{L_y}\left[\cot\theta - \frac{\partial \ln p}{\partial \tan\theta}\right]^2 K^2 F(K,\Phi) \tag{2.8}$$

where F is the two-sided, polar-symmetric height spectrum defined so that the height variance,

$$\langle\zeta^2\rangle = \int_0^\infty\int_0^\pi 2F(K,\Phi)KdKd\Phi \tag{2.9}$$

The rms modulation depth, by definition, is given by

$$\mu(\Phi) = \langle m^2(x,\Phi)\rangle^{1/2} = \left[\int_0^\infty 2P_m(K,\Phi)dK\right]^{1/2} \tag{2.10}$$

It should be pointed out that, strictly, the large footprint limiting form is valid only if L_y is much larger than the lateral decorrelation scale of $\partial\zeta/\partial x$. This is equivalent to the condition $KL_y \gg 1$ in the general case of directionally spread seas, but not in the case of unidirectional, long-crested swell. We have encountered such a swell in our aircraft experiment, where the crest length was very long compared to the antenna beamwidth. In such a case a separate calculation must be carried out, one which accounts for the curvature of the em wave front. But as the case we encountered was exceptional among our data, we have neglected to perform such a calculation.

Now it is only consistent at this point to assume that the slope pdf is Gaussian. Indeed, it would be inconsistent to assume otherwise since the tilt model is predicated on an assumption of free, non-interacting waves, and this can only imply normal statistics. The K_u-band scatterometer data of Jones et al. (1977) analyzed by Wentz (1977) show in fact that the pdf is nearly normal. More interesting though, the data indicate that the pdf at K_u-band frequencies is very nearly isotropic. This is convenient, as it simplifies the measurement of bi- or multi-modal directional spectra since the sensitivity is independent of azimuth, and no relative weighting of different directional components is required. If the slope pdf is Gaussian and isotropic, then the sensitivity coefficient, the factor of $K^2 F$ in (2.8), can be written as

$$\alpha \equiv \frac{\sqrt{2\pi}}{L_y}\left[\cot\theta + \frac{2\tan\theta}{\langle|\nabla\zeta|^2\rangle}\right]^2 \tag{2.11}$$

where $\langle|\nabla\zeta|^2\rangle$ is the mean square wave slope effective at the particular radar operatng frequency (diffraction-effective mean square slope).

The linear tilt model solution (2.8) is identical to the first term in the series expansion of the geometrical optics solution obtained by J. The second-order terms consist of a em and a hydrodynamic (hydro) term. The two terms are of comparable magnitude, both scaling as the large-wave steepness $\delta_o \equiv K_o\langle\zeta^2\rangle^{1/2}$ to the fourth power. The em term is independent of hydrodynamic nonlinearity and arises in scattering from a normally distributed sea surface. The hydro term is due to the non-Gaussian statistics associated with hydrodynamic nonlinearity, and is given in terms of various third moment statistics in wave height and slope. Since these statistics scale with δ_o (see J; also Huang and Long, 1980), the result is that both em and hydro terms scale as $\delta_o{}^4$. The calculations of the second-order em term carried out in J indicate that, firstly, the term is generally small, and secondly, that the least harmonic distortion occurs in the neighborhood of 10° incidence. The smallness of the second-order terms requires that the following inequalities should be satisfied:

$$\begin{array}{ll} \text{i)} & \delta_o \cot\theta \ll 1 \\[2ex] \text{ii)} & \dfrac{\delta_o \tan\theta}{\langle|\nabla\zeta|^2\rangle} \ll 1 \end{array} \qquad (2.12)$$

If i) is violated seriously, an obvious consequence is that the phase-front, or pulse, may intersect the surface at more than one point. A less extreme but more general consequence of violating i) is the confounding of the surface range coordinate with the wave height. The range coordinate will suffer a displacement $\delta x = \zeta\cot\theta$. The net result will be a dispersion of the range coordinate by an amount $\langle\zeta^2\rangle^{1/2}\cot\theta$. This dispersion will represent a limit to the smallest wavelengths observable by this technique. Since $\langle\zeta^2\rangle^{1/2} = \delta_o/K_o$, it follows that the upper limit on wave number as a function of the peak wave number is of the order of

$$K_{max}/K_0 \propto (\delta_0 \cot\theta)^{-1} \qquad (2.13)$$

For example, if $\theta = 10°$ and $\delta_0 = 0.05$ (fully aroused seas), then $K_{max} \sim 3.5\, K_0$. In steep developing seas, $\delta_0 \sim 0.1$, in which case $K_{max} \sim 1.75\, K_0$. To illustrate the nature of the spurious response associated with the violation of ii), take the extreme case of swell under calm conditions. Obviously, if $\tan\theta > \delta_0$ then no backscatter occurs since there are no wave slopes satisfying the specular condition. If $\tan\theta < \delta_0$, the backscatter will now occur in periodically spaced bursts at points on the swell profile satisfying the specular condition. The backscatter will look like a string of delta functions, and will bear little resemblance to the swell profile save in its periodicity. Clearly, for the measurement to have decent fidelity (to the slope spectrum) there must be sufficient small-scale roughness, or in other words, a sufficient density of specular points. Practically, this means that the local wind speed should be in excess of several meters per second.

Some guide to the selection of the 'best' incidence angle may be had by the following. Assume that the inequalities (2.12) carry equal weight, that is, assume that the consequences of violating i) and ii) are equally undesirable. Then we can minimize the sum i) + ii) with respect to θ. This yields $\tan\theta = \langle|\nabla\zeta|^2\rangle$. For example, if the wind speed is 10 ms^{-1} then using (4.8) we get $\theta = 10°$. More work along the lines established in J is required to get a better idea of what is really the best angle for minimizing the measurement nonlinearities. Unfortunately, the aircraft data are of little or no use to us here.

This is because at the relatively low aircraft altitudes, the elevation beamwidth must be fairly broad in order to generate a sufficiently large beam spot for wave number resolution. In our aircraft experiment geometry, the 10° elevation beamwidth makes it virtually impossible to establish the optimal angle since the likely range of θ lies within the beamwidth.

2.3 The short-pulse technique.

In principle, the range reflectivity modulation spectrum $P_m(K,\Phi)$ can be measured by either short-pulse or two-frequency techniques. However, as shown by J, the narrowband two-frequency technique has, inherently, a poor measurement SNR (signal-to-noise ratio) compared to the short-pulse technique. This is due to the use of narrowband waveforms that completely fill the beam. The analysis bandwidth δK in this case is equal to the reciprocal of the range footprint dimension--the 'record length'. Hence the SNR $\propto P_m(K)\delta K$ will neccessarily be small when the footprint dimension is large. Since $P_m \propto L_y^{-1}$ and $\delta K \propto L_x^{-1}$ it follows that the two-frequency SNR is inversely proportional to the footprint area as noted by Alpers and Hasselmann (1978).

In the short-pulse technique,* wide bandwidth, short pulses are used to resolve the wave structure in range. Backscattered pulses are integrated in surface-fixed range bins, and the range modulation spectrum is computed digitally from the observed sample of the range modulation $m(x,\Phi)$. For narrow pencil beams, the curvature of the wavefront can be neglected, and the surface range can be taken to be a linear function of the signal delay time τ. If the

---

*The terminology may be due to Tomiyasu (1971).

motion of the platform is accounted for, then

$$x = c\tau/(2\sin\theta) + Vt\cos\Phi \equiv x' + Vt\cos\Phi \tag{2.14}$$

where c is the speed of light, V is the platform speed, and where x and τ are referred to the center of the beam spot at $t = 0$. The coherency of the radiation results in random signal fading akin to the speckle observed when a coherent laser illuminates a 'rough' surface such as an ordinary piece of bond paper. The backscattered field statistics are complex Gaussian, the amplitude is Rayleigh-distributed, and the detected power is exponentially distributed (Moore <u>et al</u>., 1975). If the measurement integration time is short (< 1 s), the surface can be regarded essentially as frozen. Consider the backscatter of a short pulse of length $\Delta\tau$. The surface range resolution cell is given by

$$\Delta x = c\Delta\tau/(2\sin\theta) \tag{2.15}$$

It is assummed that Δx is small compared to the dominant wavelength. The backscattered power in a pulse transmitted at a time t_i can be modelled as a weakly modulated noise process of the form

$$W_i(x',\Phi) = W_o(x',\Phi)[1 + m(x,\Phi)]w(x,t_i) \tag{2.16}$$

where $W_o \propto G^2(x)\sigma^o(\theta,\Phi)$ is the average backscattered power profile profile and w is the unit exponential fading process. The decorrelation length of the w-process is equal to the range resolution; more generally, if excess bandwidth is employed, the decorrelation length is given by the reciprocal of the pulse bandwidth

(Moore et al., 1975). Since the autocorrelation function of the fluctuating component of the w-process is concentrated near the origin, it follows that the spectrum of the (normalized) backscattered power is given by

$$P_i(K,\Phi) \approx \delta(K) + P_m(K,\Phi) + [1 + \mu^2(\Phi)]P_W(K) \qquad (2.17)$$

where δ is the Dirac delta function. The fading spectrum is essentially the spectrum of the transmitted pulse. This follows since the backscattered field is given by the convolution of the pulse waveform with the surface impulse response, which, in the absence of modulation, is a complex Gaussian white noise process. For a Gaussian pulse shape with half power width $\Delta\tau$ one finds (cf. J, eqs. 5 and 70 et seq.):

$$P_W(K) = \frac{\Delta x}{2\sqrt{2\pi \ln 2}} \exp[-(K\Delta x)^2/8\ln 2] \qquad (2.18)$$

An integration of N independent pulses will reduce the fading variance by a factor of N^{-1}. Because of the platform motion, the backscattered pulses must be integrated in range bins that are fixed in the surface, otherwise the wave contrasts will be smeared out by range walk. This can be accomplished simply by delaying or advancing the trigger signal to the sampling gates according to the line-of-sight relative speed between the platform and the surface.* The N pulse average can be expressed as

$$W_N(\tau) = N^{-1}\sum_{i=1}^{N} W_i(\tau + \dot{\tau}t_i) \qquad (2.19)$$

---

*For satellites, it may prove difficult to specify the relative speed as a function of azimuth to the required accuracy. In this case, an alternative processing scheme, similar to that employed in the dual frequency technique, may have to be devised.

where the rate of change of signal delay $\dot{\tau} = -(2V/c)\sin\theta\cos\Phi$. Omitting the dc term and neglecting μ^2, then the spectrum of the N-pulse average is given by

$$P_N(K,\Phi) \approx P_m(K,\Phi) + N^{-1}P_W(K) \tag{2.20}$$

If thermal noise is negligible, then the SNR is just the ratio of the signal spectrum to the residual fading spectrum, $SNR = NP_m/P_W$. Using (2.18) for P_W and assuming $K << 2\pi/\Delta x$, we have

$$SNR = \frac{2\sqrt{2\pi \ln 2}}{\Delta x} N \, P_m(\underline{K}) \tag{2.21}$$

The number of independent pulses depends on the pulse repetition frequency (PRF), the Doppler bandwidth B_d, and the integration time T_{int}. If the PRF > $2B_d$, the signal is essentially continuously sampled and hence $N = B_d T_{int}$. If the PRF << B_d, then the individual pulses are independent, in which case $N = PRF \times T_{int}$. The Doppler bandwidth is determined by the interference rate of waves backscattered from the lateral extremities of the range resolution cell. From elementary considerations, or from equation 72 in J,

$$B_d = (2V/\lambda)\beta_\phi|\sin\Phi| \tag{2.22}$$

Here B_d is the half power, post-detection Doppler spread in Hertz, λ is the em wavelength, and $\beta_\phi \equiv (L_y^*/H)\cos\theta$ is the half-power azimuth beamwidth.

The measurement integration time is limited by the azimuth scan rate which in turn is driven by coverage requirements. The integration time should not be longer than the time it takes to move one footprint dimension. The modulation signal can only be built up coherently when the radar is viewing the same portion of the surface. When the beam moves to view a new, statistically independent patch of sea, the range modulation signal will evolve randomly, and further integration will proceed in an incoherent fashion, not only with respect to the scintillation or fading noise, but with respect to the modulation signal as well. Thus <u>both</u> P_m and P_W will be driven down as N^{-1}. Thus, as the beam moves to view a new piece of the surface, the signal strength goes down as $1/T_{int}$ while the SNR approaches an asymptotic value. Since the antenna rotation is generally more rapid than the beam's translation, the azimuth scan rate determines the choice of integration time. Let us arbitrarily require that the beam move no more than one-half of its azimuth dimension. Then the integration time is set by

$$T_{int} < \Delta\Phi/2\dot{\Phi} = \beta_\phi \csc\theta/2\dot{\Phi} \qquad (2.23)$$

An interesting consequence of (2.23) is that the SNR is independent of the footprint dimensions and hence of the antenna gain. This follows since the integration gain $N \propto T_{int} \propto L_y$, while the signal spectrum $P_m \propto L_y^{-1}$. Thus, while the azimuth beamwidth affects the modulation signal strength (weakly as $L_y^{-1/2}$) it does not affect the measurement SNR.

The number of degrees of freedom (DOF) in a measurement of $P_m(\underline{K})$ is determined by the number of elementary wave number bands $\delta K \sim 2\pi/L_x^*$ contained in the spectral estimate. For example, consider an analysis with 25% resolution. Then the DOF of the estimate is given by (Blackmann and Tukey, 1958):

$$DOF \sim 2(0.25)/\delta K \sim KL_x^*/4\pi \qquad (2.24)$$

For example, if $L_x^* = 20$ km and $K = 2\pi/200$ m then the DOF ~ 50.

3. A SATELLITE SYSTEM

These measurements can be made with a modified Seasat class radar altimeter. The pertinent Seasat altimeter characteristics are (Townsend, 1980):

Frequency:	13.5 GHz
Pulse type:	Linear FM, 1000:1 pulse compression
Pulse length:	3.2 ns compressed
Peak power:	2.0 KW
PRF:	1000 Hz
Detection:	Noncoherent square law

One can modify the Seasat altimeter* in such a way that it can perform a dual function, first as an altimeter per se, and second as a 'directional wave spectrometer'. In the conventional altimeter mode, mean altitude and wave height are determined from the delay time and broadening of the leading edge of the averaged return of nadir-directed pulses. There are several ways whereby transmitted pulses may be shared between the instrument's nadir altimeter mode and off-nadir spectrometer mode;--for example, by power dividing or time sharing. Modification would entail the addition of a separate receiving section (post IF) and microprocessor as well as a separate rotating antenna. Pulse tracking, integration and spectral analysis

---

*Unfortunately, the Seasat engineering unit is no longer available for this purpose.

functions would be incorporated in the separate microprocessor. As an example, let us consider adding a 1 m diameter, 3 rpm rotating antenna to the existing instrument. If we assume a 700 km satellite altitude and 10° nadir angle, then the measurement geometry is that of figure 1, and the relevant measurement parameters are:

Velocity: $V = 7 \text{ kms}^{-1}$
Beamwidth: $\beta_\theta = \beta_\phi = 1.6°$
Spot size: $L_x^* \sim L_y^* = 20$ km
$(L_x \sim L_y = 8.5$ km$)$
Rotation rate: $\dot{\Phi} = 360°/20$ s
Range resolution: $\Delta x = 2.8$ m (from 2.15)
Doppler bandwidth: $B_d = 18 \, |\sin\Phi|$ KHz (from 2.22)
Integration time: $T_{int} = 0.26$ s (from 2.23)

The PRF equals B_d at $\Phi \sim 3°$ of foreward or aft. For most azimuths the PRF << B_d so that the number of independent samples is given by

$$N = \text{PRF} \times T_{int} = 260 = +\,24 \text{ dB}$$

For illustrative purposes let us assume a Phillips' cutoff spectrum with a $\cos^4$ spreading factor:

$$F(K,\Phi) = \begin{cases} 0.005(4/3\pi)\cos^4(\Phi-\Phi_o)K^{-4}, & K > K_o \\ 0, & K < K_o \end{cases}$$

Assume a 200 m water wavelength and upwave/downwave looks. Let the mean square slope as a function of windspeed be given by (4.8) and let $U = 10 \text{ ms}^{-1}$. Then we have (cf. 2.8, 2.11, and 2.21):

$$P_m = (2.95 \times 10^{-4} \text{ m}^{-1})(5.67 + 9.53)^2(2.15 \text{ m}^2) = 0.15 \text{ m}$$

$$\mu = 10\%$$

$$SNR = 260 \times 0.22 = +18 \text{ dB}$$

The directional resolution given by (2.2) is $\delta\Phi = 4.7°$; but this assumes no rotation of the beam. Since the beam moves about 5° during the integration time, the actual resolution will be somewhat less. We have already calculated the DOF in the last section: DOF ~ 50. At 10° incidence, $\sigma^0 \sim +5$ dB and is very nearly independent of windspeed. A link equation assuming 3 dB in losses and a noise factor of F = 6 dB gives a signal-to-thermal-noise ratio of + 6 dB. Thus thermal noise is not a problem, even if half the transmitter power is shared with the altimeter mode.

The spectrometer mode does not require the full pulse compression. For example, a partial compression of the chirped waveform to 20 ns (17.3 m surface range resolution) would be quite adequate. The excess bandwidth, of course, is still useful for reducing the fading variance. With 20 ns resolution, something like 1024 sample gates would adequately sample the return (17.7 km of surface range). The spectrometer mode data can be merged with the altimeter mode data stream in a way that is compatible with the existing instrument's data system. For example, the spectrometer data might consist of 58 6% bandwidth spectral estimates covering the wavelength range 50-1000 m output at a nominal 4 frames per second. This data can easily be merged with the altimeter data without exceeding the 10 kbs^{-1} data rate of the existing system. Thus, on-board recording, and hence fully global coverage is possible.

The above figures clearly indicate that these measurements are feasible. Yet, have we missed something, erred in our thinking somehow? The aircraft data to be presented below convince us that we have not.

4. AIRCRAFT VALIDATION

4.1 The Fall '78 CV-990 Mission.

The Goddard K_u-band Short-Pulse Radar was built up from the Geos-3 satellite altimeter breadboard obtained from General Electric Co. in 1974, and it shares the following characteristics with the spacecraft instrument:

Frequency:	13.9 GHz
Pulse type:	Linear FM, 100:1 pulse compression
Pulse length:	12.5 ns compressed
Peak power:	2.5 KW
PRF:	100 Hz
Detection:	Noncoherent square law

Prior to 1978, the radar was flown on several aircraft missions with fixed-azimuth, variable elevation antennas. A description of the Goddard radar as it was configured in 1975 is given by Le Vine _et al_. (1977). A major breakthrough in our program occurred in 1978 when we had an opportunity to fly piggyback, free of charge, on the 1-month long, Convair-990 Nimbus-7 Underflight Mission. For this mission, one of the fixed-azimuth printed-circuit antennas was modified (by sawing it in half) and adapted to an azimuth scan. Also, the data system was redesigned to allow continuous recording at the full PRF.

Figure 4 shows the rotating antenna installed in the CV-990's instrument 'sled'. It is shown surrounded by a cylindrical baffle which was designed to protect a neighboring radiometer from possible RFI. Also shown in figure 4 is a 12° X 12°, nadir-directed rectangular horn antenna, which served in our instrument's 'altimeter' mode. The nadir horn and rotating antennas are shown connected by a waveguide switch; this switch could be activated by a mode-change command from the radar's control panel in the aircraft cabin. The rotating antenna characteristics are:

Boresight incidence angle, $\theta_o = 15.8°$
Azimuth beamwidth, $\beta_\phi = 4°$
Elevation beamwidth, $\beta_\theta = 10°$
Rotation rate, $\dot{\Phi} = 6$ rpm

The boresight angle was chosen so that an elevation sidelobe at 15.8° to the main-beam axis would be directed toward nadir. The return from the sidelobe, which was recorded in the same frame as the main-beam return, allowed us to calculate the range on the surface without having to calibrate for absolute time delay. This is important in the relatively low-altitude (10 km) aircraft geometry where a rather broad elevation beamwidth is required to generate a large enough range footprint extent for wave number resolution. Thus in the aircraft geometry, wave-front curvature in the elevation plane is not negligible, and if not properly accounted for, the curvature will result in a considerable dispersion of the surface wave number. If τ is the time elapsed from the time of the nadir sidelobe return, then given the aircraft altitude from the plane's operational altimeter, the surface range x as measured from the nadir point can be calculated according to the equation

$$x^2 + H^2 = (c\tau/2 + H)^2 \tag{4.1}$$

Of course, in the satellite measurement geometry, we can linearize (4.1) to get (2.14). The aircraft measurement geometry is illustrated in figure 5. At the nominal aircraft altitude of 10 km, the footprint dimensions are $L_x* = 1500$ m and $L_y* = 700$ m approximately. Because of the rapid roll-off of σ^0 with θ , the backscattered power peaks inward of the boresight angle. Generally, the peak return occurs in the vicinity of 13° incidence. The metallic baffle, and the poor radome environment in general spoiled the gain pattern to such an extent that we have not attempted to measure σ^0 either as a function of elevation or azimuth angle. Figure 6 is an example of the (azimuthally averaged) average backscattered power profile; the large ~ 3° ripple near the beam axis caused by diffraction by the baffle is obvious. The poor gain pattern is unfortunate as, ideally, we want to estimate the tilt model sensitivity term $\partial \ln p/\partial \tan\theta$ directly from the observed cross-section roll off. The gradient of the slope pdf and mean square slope are <u>internal</u> parameters of the measurement; yet, in the analysis to follow we shall have to rely on <u>external</u> parameters in order to calculate the tilt model sensitivity α. That is, we will have to use a mean relationship between the mean square slope and the buoy-observed wind speed in order to verify the prediction of the tilt sensitivity coefficient (2.11).

The digital data system consisted of a high-speed waveform sampler (Biomation Co.), two 6 k-byte buffers, and a high-speed (75 ips)

1600 bpi tape drive. The Biomation sample gates were selectable and could be set to 2, 5, 10, or 20 ns. Quantization was 6 bits and the maximum frame size was 1024 samples. Generally, we recorded in the spectrometer mode at a 5 or 10 ns rate, taking 512 samples at the full PRF. Shaft encoder and other housekeeping data were recorded in the first two tape tracks.

The Fall '78 Mission took in 19 flights of approximately 5 hours duration in the period October 24 - November 19, 1978. About half of these flights were over ice, the remainder over water. Approximately 50 2400 ft tapes were written with ocean backscatter data; roughly half these data were taken in the instrument's spectrometer mode, the remainder in the altimeter mode. The spectrometer files are by and large 1-2 minutes long. The 1 minute files, amounting to only [illegible] antenna rotations, are a bit short on equivalent DOF and consequently the spectra from these files are noisy.

In this paper we are only concerned with validating the technique, and so we shall be examining only a small subset of the Fall '78 Mission data set; that is, we shall only be examining those files for which we have corroborative 'surface truth'. Table 1 is a summary of the surface truth data set (spectrometer mode). This data set consists of overflights of three types of wave-recording buoys, including two NOAA data buoys (N.E. Pacific), a Waverider (Norwegian Sea), and a pitch-roll buoy (N.E. Pacific). Colocation was generally within 100 km spatially and within 1 hr temporally.

4.2 Data analysis

The digital flight tapes were reformatted and compressed by averaging

3 consecutive pulses. Also, the spectrometer mode data were standardized to 10 ns resolution. Figure 7 is an example of the backscatter data contained on the reformatted tapes. The figure shows 1500 pulse returns, intensity-coded, and stacked vertically, on a CRT display. These (essentially raw) data were further processed on a general purpose computer as follows:

1) The equally spaced array in time $W(m\Delta\tau)$, $m = 1, 2, \ldots 512$, is converted to an equally spaced array in surface range according to (4.1). The nominal surface range resolution $\Delta x = 8.1$ m at 13° incidence; however, it was more convenient to array the data in equally spaced 12 m surface range bins.

2) The geometrically corrected data are then subjected to two algorithms. In the first, no motion correction is applied; the data are smoothed in range, and averaged over the several rotations of the antenna. This produces an estimate of the average backscattered power $W_0(x,\Phi)$. In the second algorithm, the motion compensation is applied. That is, the array is transformed according to $x \leftarrow x + Vt \cos\Phi$. The data have been processed in 15° azimuth blocks; given the 6 rpm rotation rate this means we have integrated $N = 42$ independent pulses. (The pulses are generally independent even for forward/aft looks since the sea-Doppler spread is generally greater than 100 Hz.) The decision to process in 15° blocks was made some time ago; this seemed reasonable as the nominal directional resolution is about 17° (200 m wave) and tests indicated no loss of signal strength. However, this is about equal to the angle subtended by the footprint, and therefore the 15° is at odds with our prior

dictum (2.23) to allow no more than half a beamwidth's movement in azimuth. Thus, the problem of the appropriate integration time for the aircraft data is still somewhat open, and requires a second and more careful examination. (As discussed in Section 2, choosing too long an integration time will not affect the spectral shape, only the signal strength; that is, the signal strength will start to drop as the integration becomes incoherent with respect to the modulation signal. Thus, it is possible that we may have to reexamine our conclusions about the precise values of the sensitivity coefficient.)

3) The accumulated N-pulse average is normalized by the estimate of the average power $W_0(x,\Phi)$ and unity is subtracted. (The azimuthal dependence of W_0 is probably mostly due to asymmetry in the radome environment.) The data are then rewindowed by a cosine-squared window. In the high altitude range (8-10 km) the window end points are taken to be $x = 800$ m and $x = 3872$ m, and at the low altitudes (4-6 km) these values are halved. The midpoint of the window corresponds roughly to $\theta = 13.5°$.

4) Estimates of $P_N(K,\Phi)$ for each 15° azimuth block are computed using a 256 point Fast Fourier Transform. These estimates are then ensemble-averaged over the several rotations of the antenna.

Figures 8a-f are polar contour plots of the processed directional spectra $P_{42}{}^*(K, \Phi)$ in units of meters where $P_N{}^* \equiv 4\pi P_N$ is the one-sided (in K) spectrum as a function of wave number in cycles per meter. The noise background has not been subtracted in these plots, but as the SNR is quite high (+10-20 dB), the background noise level is insignificant. Thus, these spectra can be viewed as directional slope spectra (one need only supply the 'calibration constant' α). Figure 8a is the directional spectrum of a storm sea, significant wave height H_S = 9.4 m, dominant wavelength = 330 m. This spectrum (Tape 36/File 1) was produced from a long run, and hence it is very stable. Figures 8b and e are examples of bimodal spectra. Figure 8c represents a fairly low sea state (H_S = 1.9 m). The 'rattiness' of this spectrum is characteristic of the noisy spectra from the short files (< 6 rotations). Figure 8f is an interesting example. It is the observed spectrum of a unidirectional, ~ 330 m monochromatic swell running under fairly light winds. Visually, from the vantage point of 8.4 km, the sea surface had the striking appearance of a diffraction grating. The crest length was for all practical purposes infinite (> 40 km). (The eye can easily detect any deviations from a straight line.) It follows then that if the radar system's response were perfect, the observed spectrum would be a symmetrical pair of delta functions. The blossoming in figure 8f thus represents, in effect, the system transfer function (for this 330 m wave).* According to (2.2), the directional dispersion should be approximately 30° for this wave; indeed, this is the amount of dispersion seen in the spectrum. The wave number dispersion is determined by the finite range footprint dimension of 1500 m. If we figure roughly a dispersion $\delta K \sim 1/L_X{}^* \sim 7 \times 10^{-4}$ cpm, this accords with the observed wave number dispersion in figure 8f.

---

*Actually, this is the spectral window; one might also refer to figure 8f as a map of the spectral 'point spread function', to borrow a term from the visible imagery people.

Lastly, respecting figure 8, we note the asymmetry that is evident in several of the spectra. This is obviously related to asymmetry in the wave-slope distribution. What is significant here is that the asymmetry is by and large rather small, and this would indicate that, by and large, the second-order hydrodynamic effects are small.

Figure 9 is a series of cuts through the directional spectrum $P_N(K,\Phi)$ of Tape 36/File 1. The figure is intended here to show that the foreward face of the (slope) spectrum is sharply defined and stands clearly away from the residual antenna pattern energy near dc. This rather 'clean' situation will not obtain for the nondirectional spectra we shall be computing in the following.

4.3 Absolute nondirectional comparisons.

For these comparisons, we will need to take a closer look at the residual fading spectrum which must be subtracted from P_N to give the directional modulation spectrum P_m. Because of the nonlinear time-delay versus surface range relationship (4.1) that obtains in the aircraft geometry, the formula (2.18) for P_W will not be exact. The pulse spectrum in the surface wave number domain will be similar to the pulse spectrum only when there is a linear relationship between surface range and delay time. Nevertheless, (2.18) may stand as a fair approximation. If we assume as a nominal range resolution the resolution at 13.5° incidence, i.e., $\Delta x = 8.14$ m, then (2.18) gives (with $N = 42$),

$$\frac{4\pi P_W}{N} = 0.58\ [\mathrm{m}]\ \exp[-0.5(K/0.033)^2] \qquad (4.2)$$

where K is given in cpm. Figure 10 is a plot of the azimuthally-integrated value of P_N in the wave number band 0.0218-0.025 cpm (center frequency = 0.19 Hz) for several files, where the buoy-observed wind speed is used as an ordering parameter. From the plot one sees that an extrapolation of the observed P_N to zero wind speed (and hence, presumably, to zero modulation depth) yields the value of the residual fading variance predicted by (4.2). The pulse spectrum roll-off between zero wave number and 0.023 cpm (42 m wavelength) is about 20%.

With P_m computed from P_N by subtracting (4.2), the directional height-frequency spectrum $S(f,\Phi)$ is computed using the tilt model solution (2.8). Assuming the linear, deep-water dispersion relationship it follows that

$$S(f,\Phi) = (2/\alpha f)P_m(K,\Phi) \tag{4.3}$$

where S is the polar-symmetric spectrum expressed in m^2/Hz/rad. In computing (4.3), the measured modulation spectrum is symmetrized according to

$$P_m \leftarrow 0.5\left[P_m(K,\Phi) + P_m(K,\Phi+180°)\right] \tag{4.4}$$

Symmetrizing the spectrum, of course, has the advantage of doubling the DOF. The nondirectional spectrum is now computed according to

$$\begin{aligned} \bar{S}(f) &= (\alpha f)^{-1}\ (1/12)\sum_{i=1}^{12} 4\pi P_m(K,\Phi_i) \\ &\equiv 4\pi \bar{P}_m(K)/\alpha f \end{aligned} \tag{4.5}$$

As we have pointed out before, the sensitivity coefficient α should ideally be calculated on the basis of the observed cross-section roll-off, but the poor antenna gain pattern has made this virtually impossible. Thus, we will have to make do here with an indirect means of verifying the tilt-model predictions. First, let us measure α by taking the ratio of the area under the radar spectrum to the area under the buoy spectrum. That is, let

$$\alpha_{meas} = \frac{\int_{f_c}^{0.2\text{Hz}} 4\pi \overline{P}_m(K)\, d\ln f}{\int_{f_c}^{0.2\text{Hz}} S(f)\, df} \equiv \frac{\alpha H_s^2(\text{radar})}{H_s^2(\text{buoy})} \tag{4.6}$$

where f_c is a low-frequency cutoff, and the significant wave height $H_s \equiv 4\langle\zeta^2\rangle^{1/2}$ (where the low-frequency deficit is understood). The low-frequency cutoff is necessary because the antenna pattern effects can be quite severe in the nondirectional spectra computed according to (4.5). This is because the antenna pattern energy is omnidirectional and therefore makes a large contribution to the azimuthal average. This should be apparent from figures 8, 9 and 11. (Also, the 1/f factor in going to the height spectrum will magnify any errors in the specification of the fading noise background level, producing, in effect, a '1/f noise' background.)

Table 2 lists the measured alphas for 10 files, representing basically 7 independent observations. The cutoff frequency in each case is chosen arbitrarily as the frequency of the minimum between the dc and the spectral peak. Figure 11 gives five examples of the inferred directional height spectra based on the measured alphas. Figures 12a-e compare the inferred nondirectional spectra with buoy observations. The five examples shown are plotted autoscaled, linear-linear; they cover a range of sea states from $H_s = 1.9$ m to 9.4 m, and include a variety of spectral forms. It is seen that the agreement is generally excellent over the entire range from f_c to 0.2 Hz. The minor discrepancies that are apparent in some of these comparisons can be attributed, for the most part, to sampling variability, geophysical variability (colocation error), and antenna pattern contamination. One does not need to look for explanation in terms of second-order scattering effects. These effects are by and large so small as to be masked by the larger errors. For example, consider sampling variability. The 90% confidence interval on the buoy spectrum in figure 12a is $(0.6\,\bar{S},\ 1.9\,\bar{S})$. Thus the confidence interval on the peak of the spectrum is 130% of the full scale of the figure! The pattern contamination is evident in all figures, but it is only severe in the case of figure 8c. In this case, both the frequency and the spectral density are low. If one examines all the figures, it would appear that the antenna-pattern-related dc component has a spectral density of about 2 m^2/Hz in the vicinity of 0.08 Hz; this would account for the apparent discrepancy in figure 8c. Yet, there still may be a real low-frequency whitening due to second-order scattering effects (intermodulation products;--see J); however, it is not possible with the present data to distinguish the real whitening from antenna pattern contamination. One would need a much larger footprint to reduce the dc component. There does on the other hand seem to be evidence of second-order effects on the high-frequency side: these are manifest in the slightly more rapid roll-off of the radar spectrum. This apparent 'droop' is related to (2.13) and has been predicted by J. (We will defer for the moment a discussion of the colocation errors.)

From these comparisons, we conclude that the measurements can be made with good spectral fidelity. But, how about absolute spectral levels? Let us check the measured alphas. How do they compare with (2.11)? An immediate check on the $1/L_y$ dependence is possible with files 89/2 and 89/3. The ratio of the altitudes is 9.3/4.5 = 2.07; the ratio of the alphas is 4.90/2.47 = 1.98 (a 4% difference). Thus, the asymptotic $1/L_y$ dependence is verified. Now, using (2.11) let us <u>infer</u> a mean square slope from the measured alphas. Let us assume a nominal incidence angle of 13°. Then, inverting (2.11) we obtain

$$\langle|\nabla\zeta|^2\rangle = \frac{2 \tan 13^\circ}{\left[\frac{L_y \alpha_{meas}}{\sqrt{2\pi}}\right]^{1/2} - \cot 13^\circ} \qquad (4.7)$$

The inferred mean square slope values are tabulated in Table 2 and plotted in figure 13 as a function of the buoy-observed wind speed. No corrections were made for anemometer height or atmospheric stability. An eyeball regression yields the relationship

$$\langle|\nabla\zeta|^2\rangle = 0.0028\ U\ [\mathrm{ms}^{-1}] + 0.009 \qquad (4.8)$$

for the wind speed range of approximately 5 to 20 ms^{-1}. Equation (4.8) is in perfect agreement with the K_u-band scatterometer data analyzed by Wentz (1977), at least up to the largest wind speed (12 ms^{-1}) in Wentz's data set. In fact, Wentz's data are not plotted because they are sensibly no different, and would only clutter the plot. Equation (4.8) also agrees with Wilheit's (1979) analysis of passive microwave data. It predicts slope variances that are ~ 60% of the optical values reported by Cox and Munk (1954) and which, interestingly, lie between their 'clean' and 'slick' surface observations. Our inferred mean square slope values (4.8) are thus consistent with our knowledge of what the K_u-band effective slopes should be and strongly support our conclusion that the tilt model solution (2.8) is a correct first-order relationship.*

Now let us use the regression result (4.8) in (2.11) to compute a 'theoretical' alpha. The 'theoretical' alpha can then be used to compute a 'radar-inferred' absolute height spectrum and significant wave height. Table 2 is a tabulation and figure 14 is a plot of the results for the 'inferred' wave height for the seven independent cases analyzed. Over the wave height range 1.9 m to 9.4 m the mean difference between the radar-inferred and buoy H_s is 0.00 m (sic) and the rms difference is 0.16 m. This is truly remarkable considering that a) we are using only a first-order, back-of-the envelope theory, b) our measurement geometry is not ideal (broad elevation beamwidth), c) we have had to rely on external parameters (buoy wind speeds) rather than internal parameters (cross-section roll-off), and lastly, d) the data are subject to sampling variability as well as geophysical variability (colocation errors). Some information as to the last source of error is available to us through the instrument's altimeter mode. The altimeter mode algorithm consisted of epoch realignment, and an iterative least-squares fitting of an error function to the leading edge of the average pulse return. H_s was computed from the measured temporal dispersion σ according to

---

*A factor of two error in the computation of P_m from the FFT led to the wrong result for mean square slope in Jackson et al. (1981).

$$H_s = [4c^2\sigma^2 - H_p{}^2]^{1/2} \tag{4.9}$$

where $H_p = 4.91$ m (compare with Fedor et al., 1979). The altimeter wave heights are shown in the last column of Table 2 and are plotted in figure 15. The altimeter H_s show a positive correlation with the spectrometer-mode minus buoy H_s residuals indicating that colocation errors are a significant component of the error budget. This probably explains the discrepancy in the bimodal spectrum comparison of figure 12e. However, there does remain the possibility that the sensitivity coefficient is not truly isotropic. Data from future flights with an improved radome should enable us to resolve this question.

4.4 Directional comparison.

The single directional comparison available to us is with a pitch-roll buoy deployed by NOAA from the Canadian vessel Quadra occupying Ocean Weather Station PAPA in the Pacific. Five directional spectra obtained from the buoy near the time of overflight were provided to us by the NOAA Atlantic Oceanographic and Meteorological Laboratories. Two radar files, 89/2 and 89/3, are available for comparison, but 89/3 is preferred because of its greater length, even though it is at the lower altitude. The directional height spectrum from 89/3 is shown in figure 11d, and the nondirectional comparison is made in figure 12d. Because of the basic 180° ambiguity in the radar spectrum, a true direction of wave travel must be assumed if first harmonics are to be compared. (As suggested by W. J. Pierson (personal communication), probably the most objective way to compare the buoy and radar data is on the basis of the first two angular harmonics since these are linearly related to the slope auto- and cross-spectra obtained from the buoy record.) To facilitate the comparison, the radar spectrum is set identically equal to zero in the half space which the buoy indicated to be opposite to the direction of dominant wave travel. Because the sea is rather broadly spread in this case (apparently due to wind turning) and because there is swell running at ~ 90° to the dominant wave direction, this ad hoc procedure will necessarily result in some error, particularly at the low swell frequencies.

The amplitudes and phases of the first and second harmonics of the angular distribution are compared to the buoy data in figure 16. The reason that there is a bias in direction is apparently due to the fact that the buoy's compass card had slipped, and true direction was figured after the fact from the general meteorological conditions (W. Mcleish, personal communication). There is evidently good agreement in first harmonic amplitudes from the peak to 0.2 Hz, but the second harmonic amplitudes disagree by almost a factor of two over most of the range. Why? Our guess is that the problem is with the buoy, but the reader may judge for himself. A standard practice in the analysis of pitch-roll buoy data is to assume a model angular distribution function such as the following

$$D(f,\phi) = \cos^{2s}[(\phi-\phi_o)/2] \tag{4.10}$$

The first and second harmonics of this distribution can then be equated to the observed first and second harmonics to give two estimates, s_1 and s_2, of the spreading parameter s as a function of frequency (Cartwright, 1963). If the two s-parameters are identical, then the actual angular distribution is perfectly represented by the model function (4.10). Figure 17 is a plot of the two s-parameters for the radar data. They are practically equal over the entire range of frequencies. This makes sense since, according to figure 18, the radar data do appear to be consistent with a cosine-power distribution. But now, the buoy data do not appear to be consistent with a cosine-power model. This is apparent from figure 19, which shows the radar data falling neatly on Cartwright's (1963) curve while the buoy data scatter over a large area above the curve.

This consistency of the radar data versus that of the buoy data naturally inclines us to believe more in the radar results, especially as we are biased in that direction to begin with. Nonetheless, we should avoid drawing hasty conclusions. In truth, the disagreement here is not as great as figure 19 might lead one to believe. First, recall that there is agreement in the first harmonic and s_1 values. At the peak, $s_1 = 4.9$, which implies a half-power spread of 85°. Second, the half-power spread is not very sensitive to the s-value, at least for $s > 5$ or so. While the buoy s-values scatter considerably, they average about $s_2 = 10$ near the peak. This implies a spread of 59° which, really, is not that far away from 85°. Further, the average of the two values, 72°, is quite close to the observed radar half-power spread of 67° at 0.114 Hz.

Still, we are skeptical of obtaining from buoys the kind of intercomparison data we need to gain a full understanding of the limits of accuracy of these radar measurements, especially as concerns the radar's ability to measure directional spectra of complex seaways. Another new aircraft radar development, the NASA Surface Contour Radar (Walsh et al., 1981), promises to be able to provide exactly the kind of high-resolution intercomparison data we now require at this point.

5. CONCLUSION

We have described a rather simple microwave radar technique for measuring directional wave spectra. We have shown that satellite measurements on a truly global scale are possible with this technique nique, and we have, in our opinion, provided a firm theoretical and experimental basis for the technique. While further aircraft experimentation is warranted and desirable we are going to be limited by the constraints of the relatively low aircraft altitudes. That is, at aircraft altitudes in a near-nadir geometry, there is no way to avoid both a relatively broad beamwidth on the one hand and a relatively small footprint on the other. Both of these factors make it difficult to investigate second-order scattering effects: we may have the theory, but we will be unable to satisfactorily verify it. Without a space experiment, there is little reason to develop the theory of measurement any further; that is, to go beyond Jackson's (1981) theory.

We do intend however to improve the aircraft radar system. For example, we are replacing the 12° nadir horn antenna with a much broader-beamwidth standard gain horn. This should permit accurate measurements of the isotropic cross-section roll-off and mean square slope for better estimates of the first-order sensitivity coefficient. This type of measurement has been described by Hammond et al. (1977).

ACKNOWLEDGEMENTS

Dr. J. E. Eckerman initiated the Goddard 'Short Pulse Radar' program nearly a decade ago, and for many years he was the motivating force behind it. In 1974, he got ahold of the Geos-3 breadboard altimeter and hired one of us (W.T.W.) to make a working radar of it; subsequently, he hired another of us (F.C.J.) to figure out how and why it should be working. We can only hope that the accomplishment of the present work in some measure releases us from a non-trivial debt of gratitude.

The cooperation of the following individuals and institutions is also gratefully acknowledged: P. Gloersen, NASA Goddard Space Flight Center; E. Peterson, NASA Aimes Research Center, and the crew of the CV-990 aircraft, the 'Galileo II'; S. Renwick, NOAA Data Bouy Office; S. Tryggstad, director, VHL River and Harbour Laboratory, Trondheim, Norway; and D. Ross and W. McLeish, NOAA Atlantic Oceanographic and Meteorological Laboratories, Miami, Florida.

We thank T. Wilheit for a helpful suggestion; also, the contributions of J. McArthur, Applied Physics Laboratory, C.Y. Peng, Science Systems and Applications Inc., and K. Tolbert, Computer Sciences Corporation, are acknowledged.

For the past three years this work has been supported by Supporting Research and Technology funding from the Oceanic Processes Branch of NASA Headquarters. We should like to thank W. S. Wilson and

L. F. McGoldrick of the Oceanic Processes Branch for their support, and especially their patience this last year in awaiting these results.

Lastly, we thank the referees for their valuable criticism, especially the referee who, despite the fact that he knew 'all that radar stuff', found the original MS cryptic and incomprehensible. While irksome, this criticism was taken to heart. In the process of revision we made many improvements and corrections which otherwise might never have been made, or which might have, but on a much longer time scale.

REFERENCES

Alpers, W., and K. Hasselmann, 1978. The two-frequency microwave technique for measuring ocean wave spectra from an airplane or satellite, *Boundary-Layer Meteorol.*, *13*, 215-230.

Beal, R. C., P. S. Deleonibus, and I. Katz (editors), 1981. *Spaceborne Synthetic Aperture Radar for Oceanography*. The Johns Hopkins University Press, Baltimore and London, 215 pp.

Blackmann, R. B. and J. W. Tukey, 1958. *The Measurement of Power Spectra*, p. 21, Dover Publication, Inc., New York.

Brown, G. S., 1978. Backscattering from a Gaussian - distributed perfectly conducting rough surface. *IEEE Trans. Antennas Propagat., AP-26*, 472-482.

Cartwright, D. E., 1963. The use of directional spectra in studying the output of a wave recorder on a moving ship. In *Ocean Wave Spectra*, pp. 203-218, Practice-Hall, Inc., Englewood Cliffs, N.J.

Cox, C. and W. Munk, 1954. Measurement of the roughness of the sea surface from photographs of the sun's glitter, *J. Opt. Soc. Am.*, *44*, 838-850.

Fedor, L. S., T. W. Godbey, J. F. R. Gower, R. Guptill, G. S. Hayne, C. L. Rufenach, and E. J. Walsh, 1979. Satellite altimeter measurements of sea state - an algorithm comparison, *J. Geophys. Res.*, *84*, 3991-4002.

Hammond, D. L., R. A. Mennella, and E. J. Walsh, 1977. Short pulse radar used to measure sea surface wind speed and SWH. *IEEE Trans. Antennas Propagat.*, *AP-25*, 61-67.

Huang, N. E. and S. R. Long, 1980. An experimental study of the surface elevation probability distribution and statistics of wind-generated waves, *J. Fluid Mech.*, *101*, 179-200.

Jackson, F. C., 1981. An analysis of short pulse and dual frequency radar techniques for measuring ocean wave spectra from satellites, *Radio Science*, *16*, 1385-1400.

Jackson, F. C., W. T. Walton, and P. L. Baker, 1981. Directional spectra from air- and spaceborne radars. In *Directional Wave Spectra Applications*, edited by R. L. Wiegel, pp. 299-314, Am. Soc. Civil Eng., New York, N.Y.

Johnson, J. W., W. L. Jones, and D. E. Weissman, 1981. Two-frequency (Δk) microwave scatterometer measurements of ocean wave spectra from an aircraft. In *Oceanography from Space*, edited by J. F. R. Gower, pp. 607-616, Plenum Press, New York and London.

Jones, W. L., L. C. Schroeder and J. L. Mitchell, 1977. Aircraft measurements of the microwave scattering signature of the ocean. *IEEE J. Oceanic Eng.*, *OE-2*, 52-61.

Levine, D. M., W. T. Walton, J. Eckerman, R. L. Kutz, M. Dombrowski, and J. E. Kalshoven, Jr., 1977. GSFC Short pulse radar, JONSWAP-75, NASA TN D-8502.

Moore, R. K., L. J. Chastant, L. J. Porcello, J. L. Stevenson, and F. T. Ulaby, 1975. Microwave remote sensors. In Manual of Remote Sensing, Vol. I, pp. 399-537, Am. Soc. Photogram., Falls Church, Virginia.

Tomiyasu, K., 1971. Short pulse wide-band scatterometer ocean surface signature. IEEE Trans. Geoscience Electron., GE-9, 175-177.

Townsend, W. F., 1980. An initial assessment of the performance of the Seasat-1 radar altimeter, IEEE J. Oceanic Eng., OE-5, 80-92.

Valenzuela, G. R., 1978. Theories for the interaction of electromagnetic and ocean waves--a review, Boundary-Layer Meteorol., 13, 61-85.

Walsh, E. J., D. W. Hancock, III, D. E. Hines, and J. E. Kenney, 1981. Surface contour radar remote sensing of waves. In Directional Wave Spectra Applications, edited by R. L. Wiegel, pp. 281-298. Am. Soc. Civil Eng., New York, N.Y.

Wentz, F. J., 1977. A two-scale scattering model with application to the JONSWAP '75 aircraft microwave scatterometer experiment. NASA Contractor Rpt. 2919, Contract NAS1-14330, Dec. 1977.

Wilheit, T. T., 1979. The effect of wind on the microwave emission from the ocean surface at 37 GHz, J. Geophys. Res., 84, 4921-4926.

TABLES

Table 1. Fall '78 Mission Surface Truth Data Summary (Spectrometer Mode).

Flt.	Tape/ File	Date (1978)	GMT		(mean) Lat.		Alt. [km]	Hdg. [°T]	Buoy ID[a]	GMT	H_s [m]	Wind speed[b] [ms^{-1}]	Wind dir.[b] [°T]	Colocation		Note
			Start	Stop	Lat. [degrees	Lon. .min]								Dist. [km]	Time [hrs]	
6	27/1	10/30	1801:13	-04:32	71.35 N	18.02 E	5.7	248	TROMSO	1725	4.2	10.1	330	3	0.6	c
7	29/1	11/01	0840:12	-42:20	72.38	23.10	9.5	051	"	0825	2.4	4.6	240	100	0.3	c
9	36/1	11/03	0811:45	-18:32	71.16	18.09	9.4	247	"	0831	9.4	18.4	280	13	0.3	
10	45/2	11/06	0950:00	-50:45	71.12	18.56	9.5	356	"	0818	3.1	11.5	190	11	1.5	
11	-/3	"	0954:30	-55:30	71.46	19.14	"	011	"	1118	2.8	"	"	10	1.4	
									"	1132	2.3	"	"		1.6	
17	85/10	11/17	0001:30	-02:30	42.14	131.45 W	9.6	071	EB-16	0000	2.2	7.9	325	14	0.0	
"	86/4	"	0036:49	-37:45	45.11	130.45	9.5	345	EB-21	0000	1.9	6.1	009	29	0.6	
"	-/6	"	0049:15	-50:15	45.53	129.56	9.5	091	"	"	"	"	"	83	0.8	
18	89/2	"	2135:30	-36:30	50.00	145.05	9.3	267	PAPA	2104	3.5	8.8-12.9	130	6	0.5	d
"	89/3	"	2142:45	-44:15	50.10	145.35	4.5	96	"	2138	3.3	"	"	42	0.0	d
"	90/7	11/18	0000:30	-01:30	46.18	131.31	8.4	134	EB-21	0000	1.3	5.7	189	41	0.0	e
"	-/9	"	0007:00	-07:46	45.52	130.27	8.4	104	"	"	"	"	"	14	0.1	e
19	91/6	11/19	2026:40	-27:40	45.36	131.37	8.7	232	"	2100	4.2	14.4	003	65	0.6	
"	94/2	"	2315:40	-17:14	41.51	128.55	8.7	128	EB-16	2400	4.0	10.3	333	119	0.7	

---

[a] TROMSO = Waverider buoy, weather station Tromsoflaket, 71.5°N, 19.0°E.
EB-16 = NOAA data buoy 46002, 42.5°N, 130°W.
EB-21 = NOAA data buoy 46005, 46.0°N, 131°W.
PAPA = NOAA pitch-roll buoy, weather station PAPA, 50.0°N, 145.0°W.

[b] Wind speed and direction at nearest 3-hourly reporting time (no height or stability corrections applied).

[c] Unresolved data problem (possibly high A/D bias level).

[d] Wind speed = 8.8 ms^{-1} at 2138Z; 12.9 ms^{-1} at 2029Z.

[e] Unidirectional, monochromatic swell--Eq. (2.8) not applicable; see text.

ORIGINAL PAGE IS
OF POOR QUALITY

Table 2. Measured Versus "Theoretical" Sensitivity Coefficient.

Radar Tape/File	Low-frequency cutoff f_c [Hz]	Measured $\sqrt{\alpha H_s}$	Buoy H_s [m]	α_{meas} [m^{-1}]	Inferred $<\vert\nabla\zeta\vert^2>$	α_{theo} [m^{-1}]	Inferred H_s [m]	Altimeter mode H_s [m]
36/1	0.055	10.90	9.4	1.34	0.061	1.36	9.35	--
45/2	0.070	4.55	3.1	1.64	0.041	2.27	2.97	2.52
		} 4.47	2.8 } 2.95					
-/3	0.067	4.39	2.3					
85/10	0.080	4.16	2.2	3.58	0.030	3.42	2.25	2.31
86/4	0.090	3.72 } 3.80	1.9	4.00	0.028	4.57	1.78	--
-/6	0.085	3.86						
89/2	0.090	4.87	3.1[a]	2.47	0.039 } 0.041	2.48[b]	3.09	3.1[a]
-/3	0.085	6.86		4.90	0.042	5.12[b]	3.03	
91/6	0.060	6.29	4.2	2.24	0.044	1.92	4.54	4.78
94/2	0.055	6.38	4.0	2.74	0.041	2.81	3.80	3.66

[a] H_s with energy below f_c subtracted (ΔH_s = -0.2 m).
[b] Average windspeed of 10.9 ms^{-1} assumed.

Mean ΔH_s = 0.00 m
Rms ΔH_s = 0.16 m

ORIGINAL PAGE IS
OF POOR QUALITY

FIGURE CAPTIONS

Figure 1. a) Typical satellite measurement geometry. b) Scan pattern on the ocean surface, 700 km altitude, 10° incidence angle, and 3 rpm scan rate.

Figure 2. Illustrating directional selectivity by phase-front matching of em and ocean wave components. For the rectangular illumination pattern illustrated here the angle of the first null is as indicated.

Figure 3. Simple tilt model of reflectivity modulation.

Figure 4. Antennas mounted in the CV-990 instrument "sled". View is upward, looking into the sled with the radome cover removed. The rotating antenna is surrounded by a cylindrical baffle. The nadir-pointing horn antenna is connected to the rotary antenna by a wave guide switch. The other antennas shown belong to the SMMR Simulator microwave radiometer.

Figure 5. Aircraft measurement geometry a) elevation view, b) plan view.

Figure 6. Azimuthally-averaged, average backscattered power profile, Tape 37/File 1. The upper and lower dashed curves represent respectively the average maximum and minimum values over 360° of azimuth.

Figure 7. CRT display of 3-pulse average backscatter data. The sample gate setting is 10 ns and the frame size is 512. The display represents 512 consecutive 3-pulse averages stacked vertically. The tic marks are placed every 250 pulses, or, equivalently, every 90° of antenna rotation. The "S" pattern is the result of antenna rotation combined with aircraft motion.

Figure 8. Polar contour plots of the (one-sided) directional spectra $4\pi P_{42}(K,\phi)$ in units of meters. Top of the figures is zero degrees radar azimuth = aircraft heading. The wave number rings are spaced every 0.005 cpm (first ring, 200 m wavelength, second 100 m, and third 66.7 m). The labeled contour level (CLEV) increments are low by a factor of 2; they should read for a) Tape/File = 36/1, CLEV = 9.08 m, b) Tape/File = 91/6, CLEV = 5.00 m, c) Tape/File = 85/10, CLEV = 3.00 m, d) Tape/File = 89/3, CLEV = 5.16 m, e) Tape/File = 94/2, CLEV = 3.76 m, and f) Tape/File = 90/7, CLEV = 2.8 m.

Figure 9. Radial cuts through the directional spectrum of Figure 8a.

Figure 10. Estimation of the background fading noise level. The level of the azimuthally averaged directional spectrum in the wave number band 0.0218-0.0250 cpm for 12 files is plotted versus buoy-observed wind speed. The data from the adjacent files 45/2 & 3, 86/4 & 6, 89/2 & 3, and 90/7 & 9 have been averaged together. An eyeball extrapolation to zero wind speed yields the value of the residual fading variance spectrum predicted by equation 4.2

Figure 11. Polar-symmetric directional height spectra $S(f,\Phi)$ corresponding to figures 8a-e. The frequency rings are 0.1 H_z and 0.2 Hz. The equally-spaced contour levels (CLEV), in units m^2/Hz/rad, have been multiplied by a factor of 2π.

Figure 12. Comparisons of radar-inferred (solid line) and buoy (circles) nondirectional height spectra S(f) using the measured alphas. a-e) correspond to a-e) of figure 11. In d) the circles and squares stand for the buoy records at 2138 Z and 2104 Z respectively. The 2138Z data have been smoothed by a 2-point average in the vicinity of the peak.

Figure 13. Mean-square slopes inferred from the measured alphas versus wind speed.

Figure 14. Radar-inferred versus buoy significant wave height (spectrometer mode). Data from adjacent files have been averaged together; cf. Table 2.

Figure 15. Radar-inferred versus buoy significant wave height (altimeter mode).

Figure 16. First and second harmonics of radar angular distribution compared to pitch-roll buoy data. Solid line (____)is from radar file 89/3; dashed (----) is from average of five buoy records; and dotted (····) is from buoy record at 2104 Z. a,b) phases; c,d) amplitudes.

Figure 17. Radar-observed spreading parameters corresponding to the first and second harmonics shown in figure 16.

Figure 18. Radar-observed directional distributions (Tape/File = 89/3) compared to cosine-power distribution. The symmetrized radar distribution is set identically equal to zero between 0° and 180°.

Figure 19. Radar (bullets) and buoy (open circles) first and second angular harmonic amplitudes compared with theoretical relationship of Cartwright (1963). The data, from radar file 89/3 and buoy record 2104Z, are contained in the frequency range 0.078 Hz to 0.145 Hz.

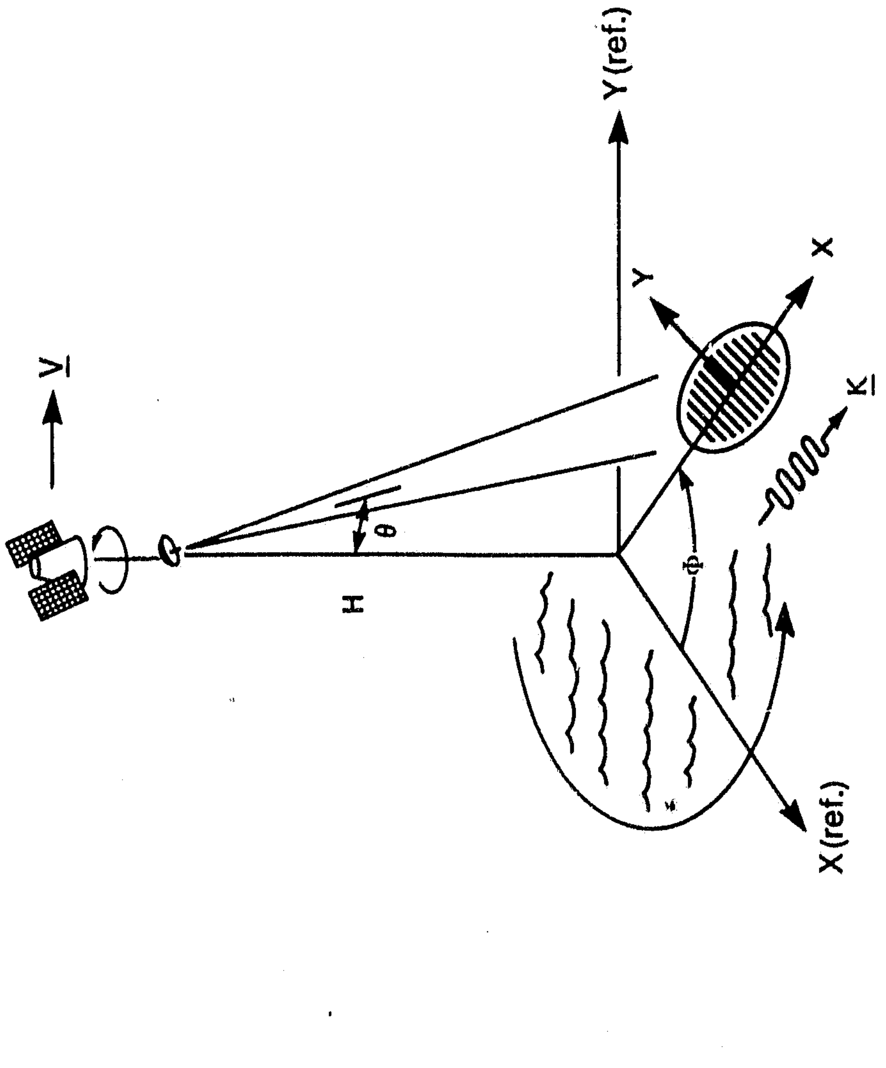

FIGURE 1a

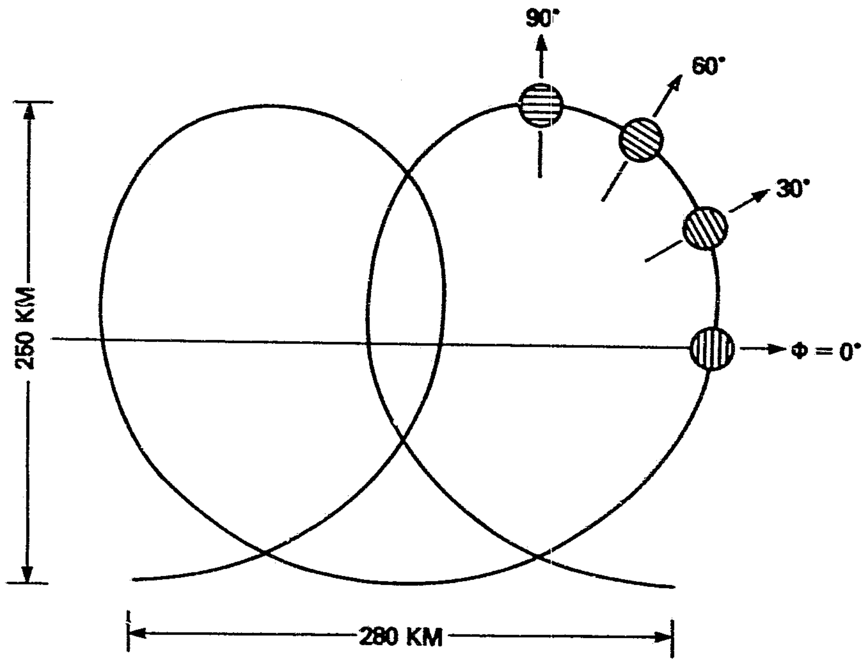

FIGURE 1b

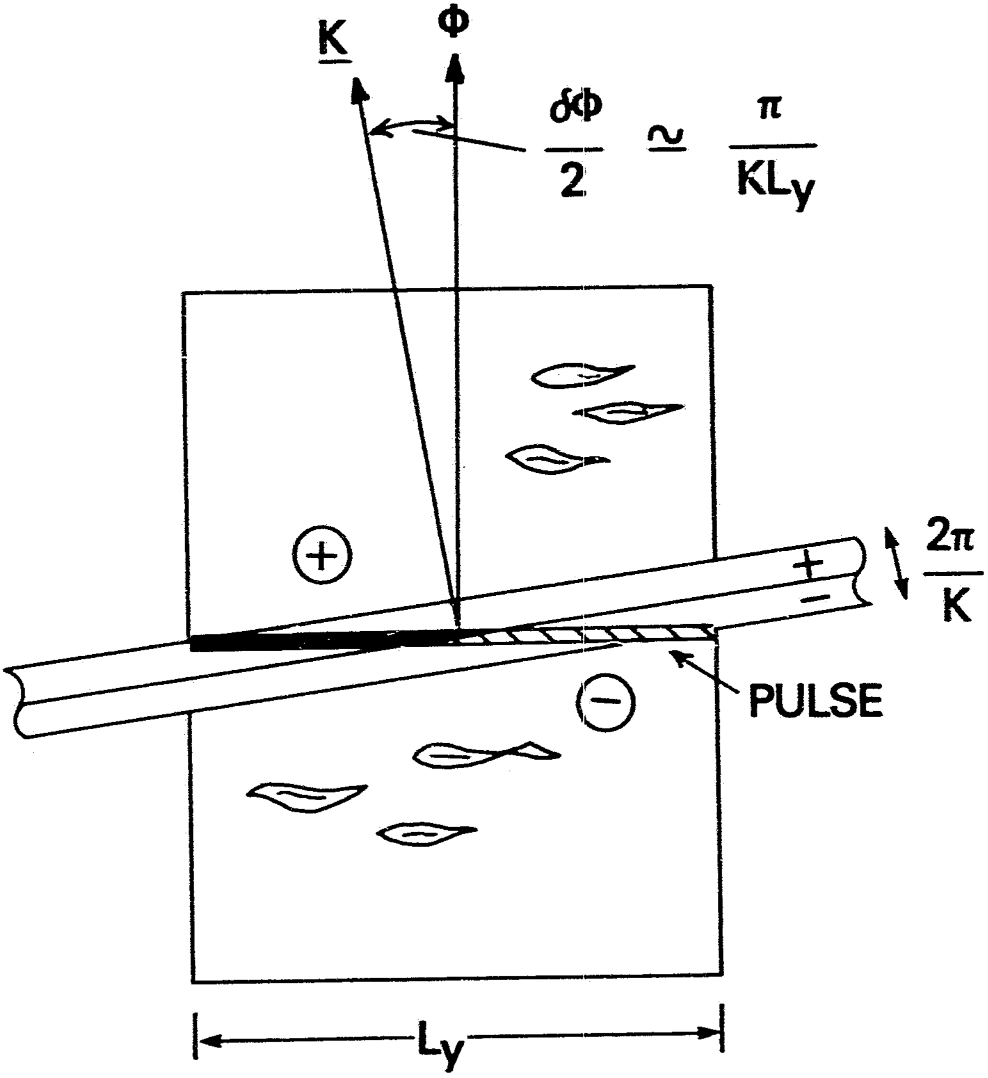

FIGURE 2

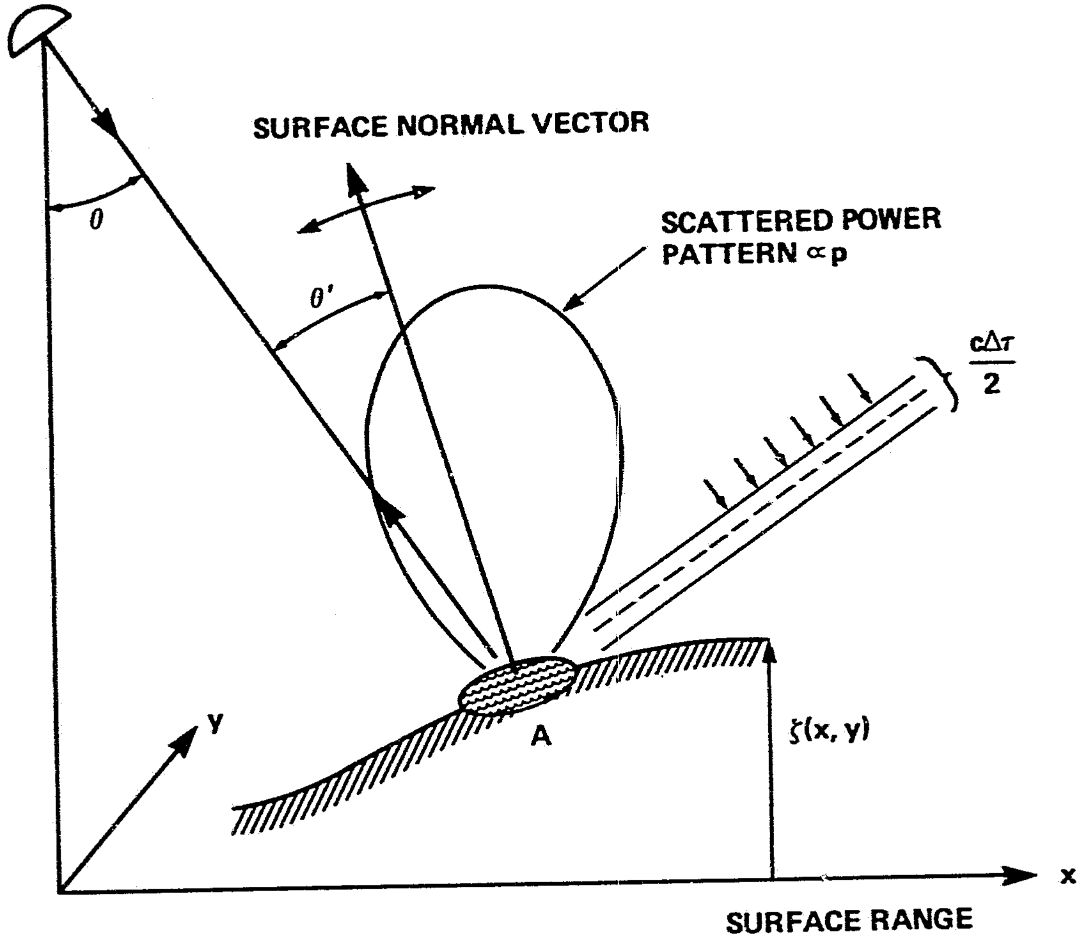
SURFACE NORMAL VECTOR
θ
θ'
SCATTERED POWER PATTERN $\propto p$
$\frac{c\Delta\tau}{2}$
y
A
$\zeta(x, y)$
x
SURFACE RANGE

FIGURE 3

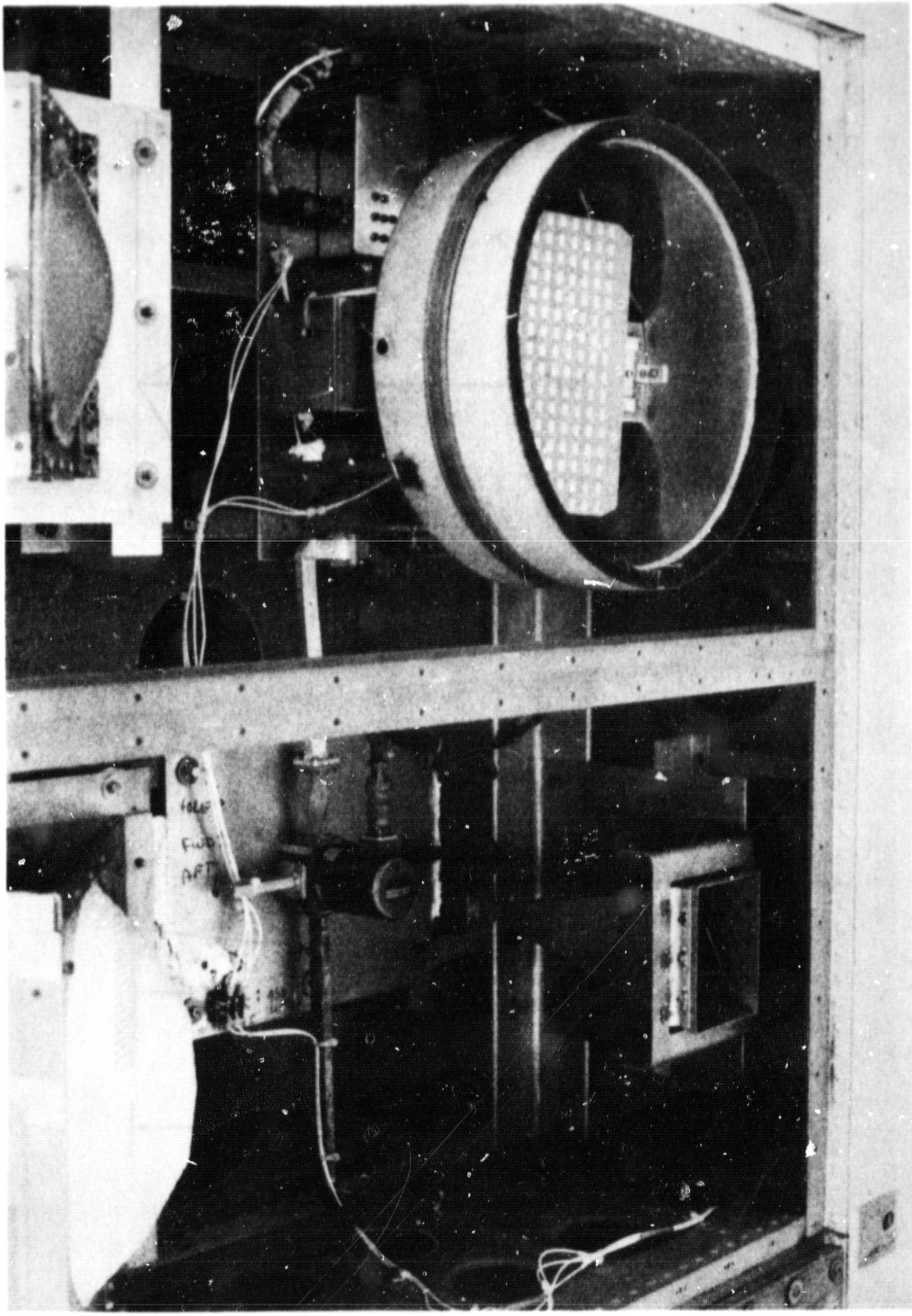

FIGURE 4

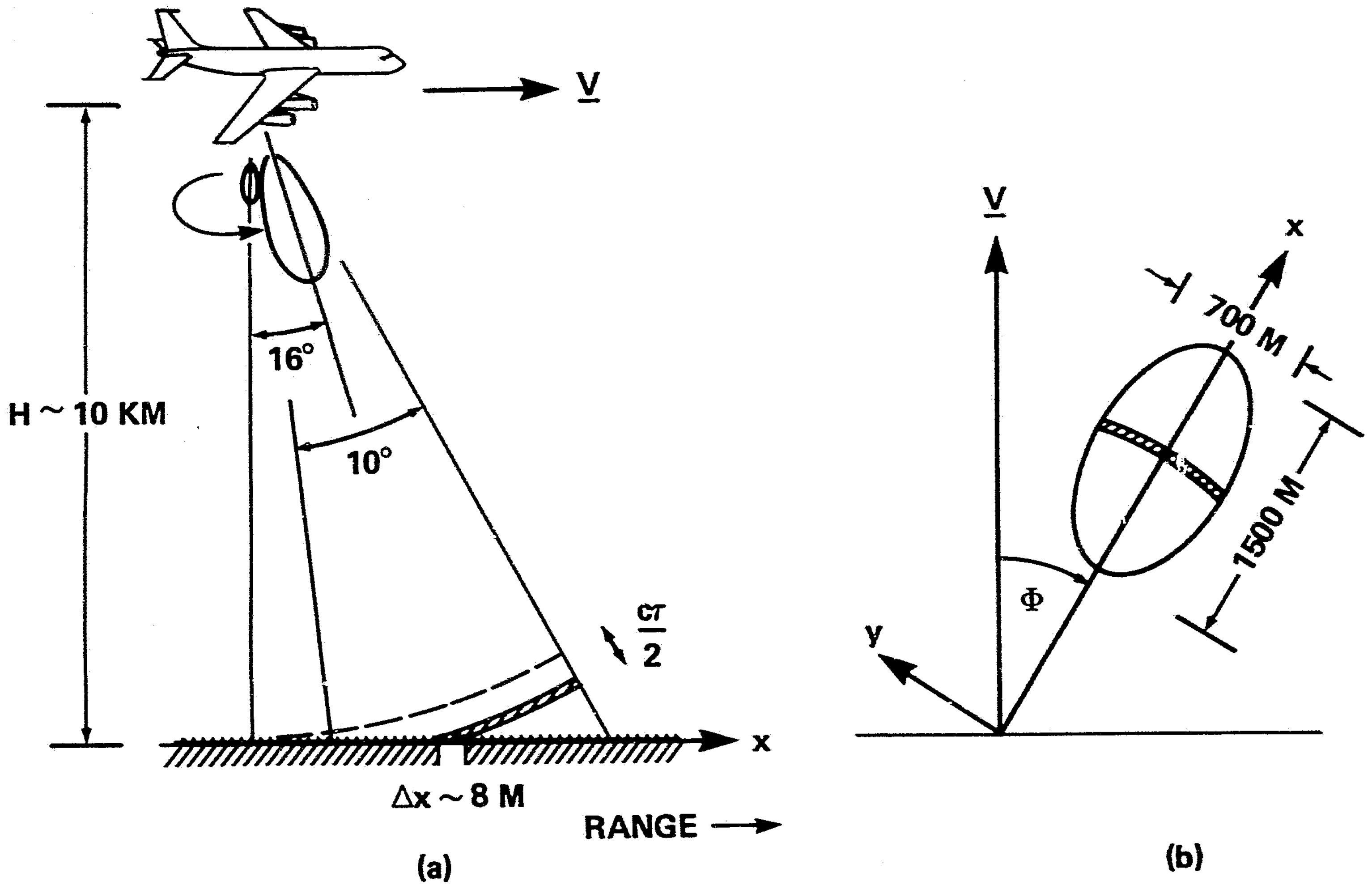

FIGURE 5

ORIGINAL PAGE IS
OF POOR QUALITY

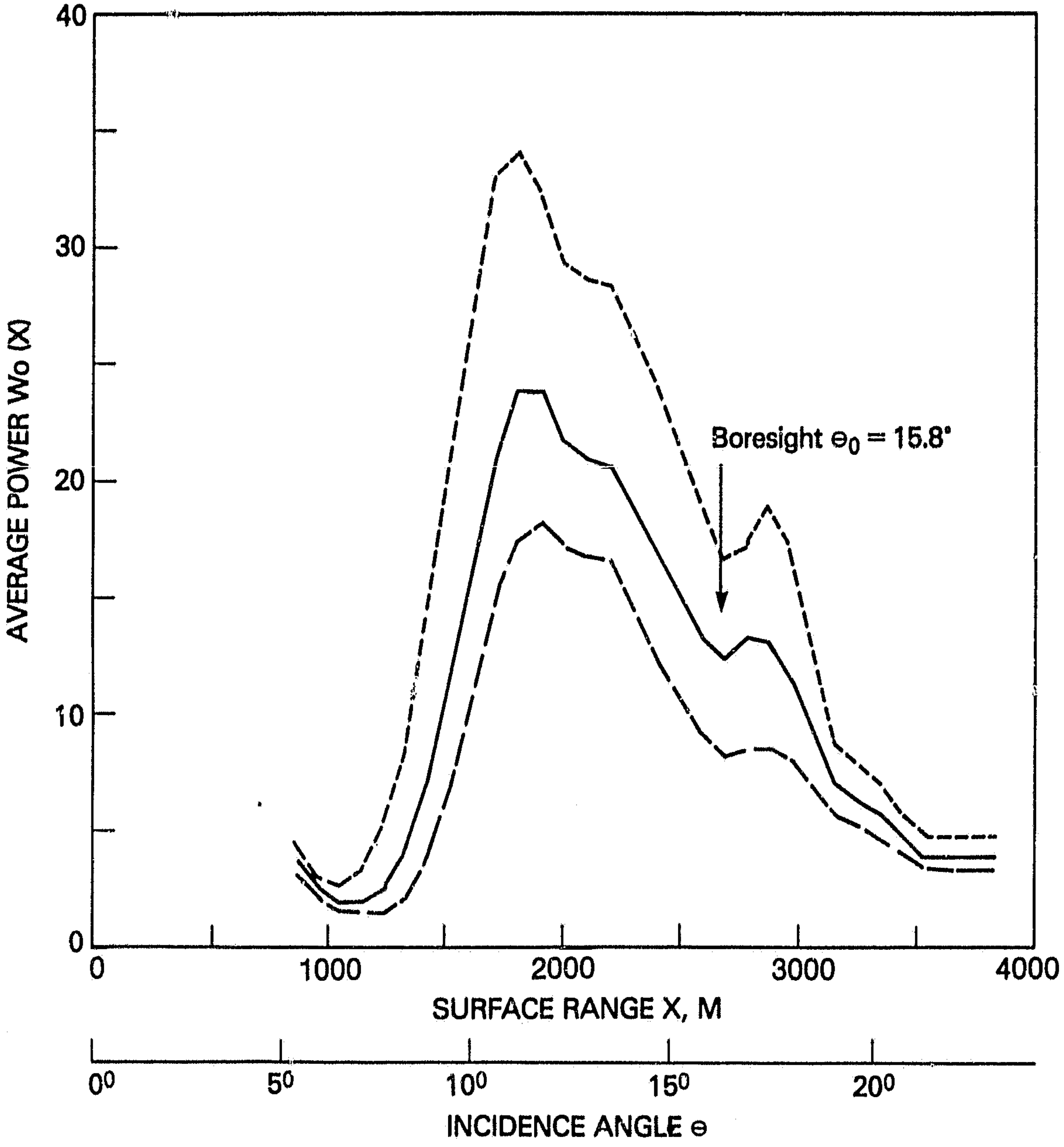

FIGURE 6

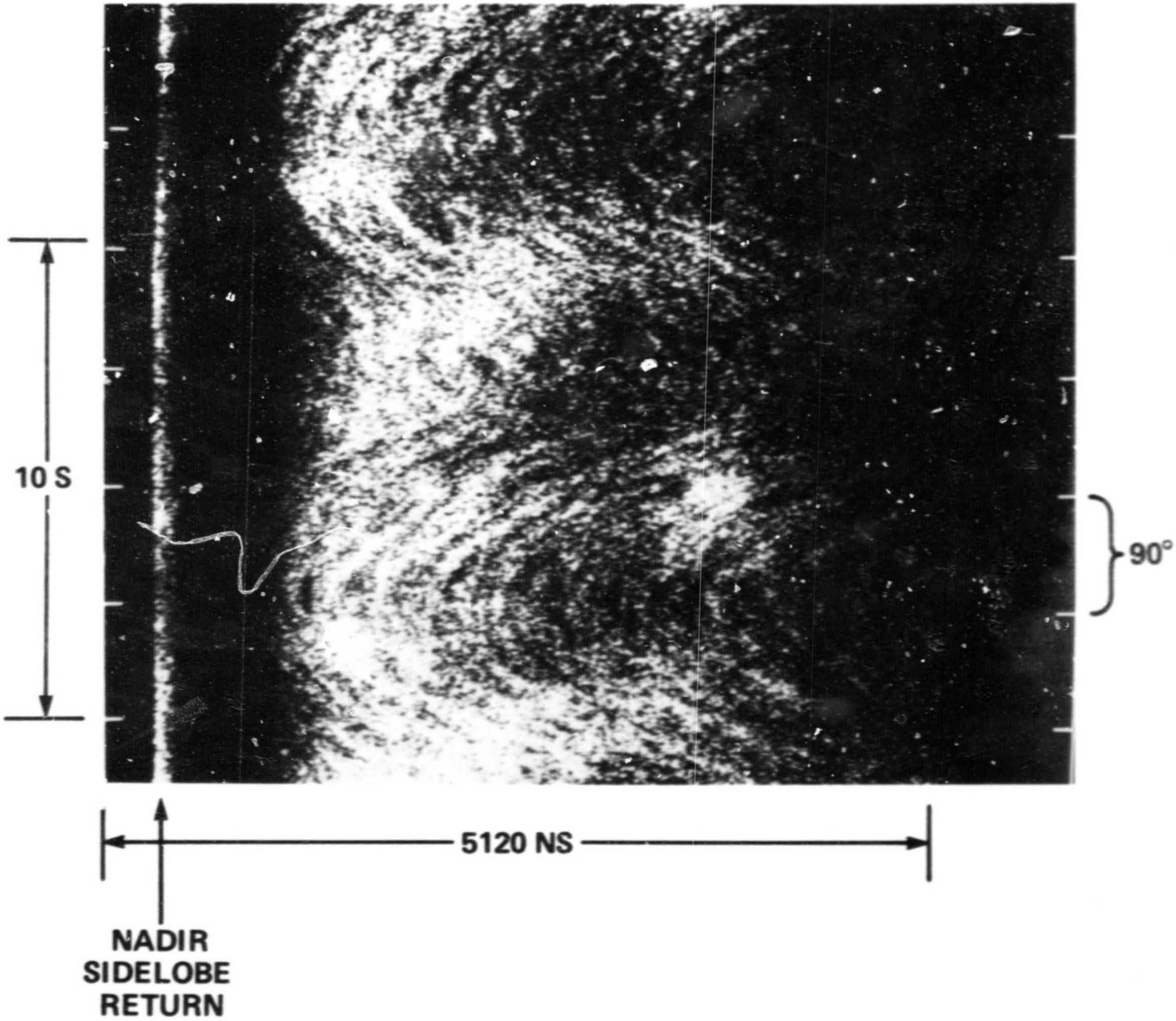

FIGURE 7

ORIGINAL PAGE IS
OF POOR QUALITY

FLT-9 TAPE367 FILE-1 ROT

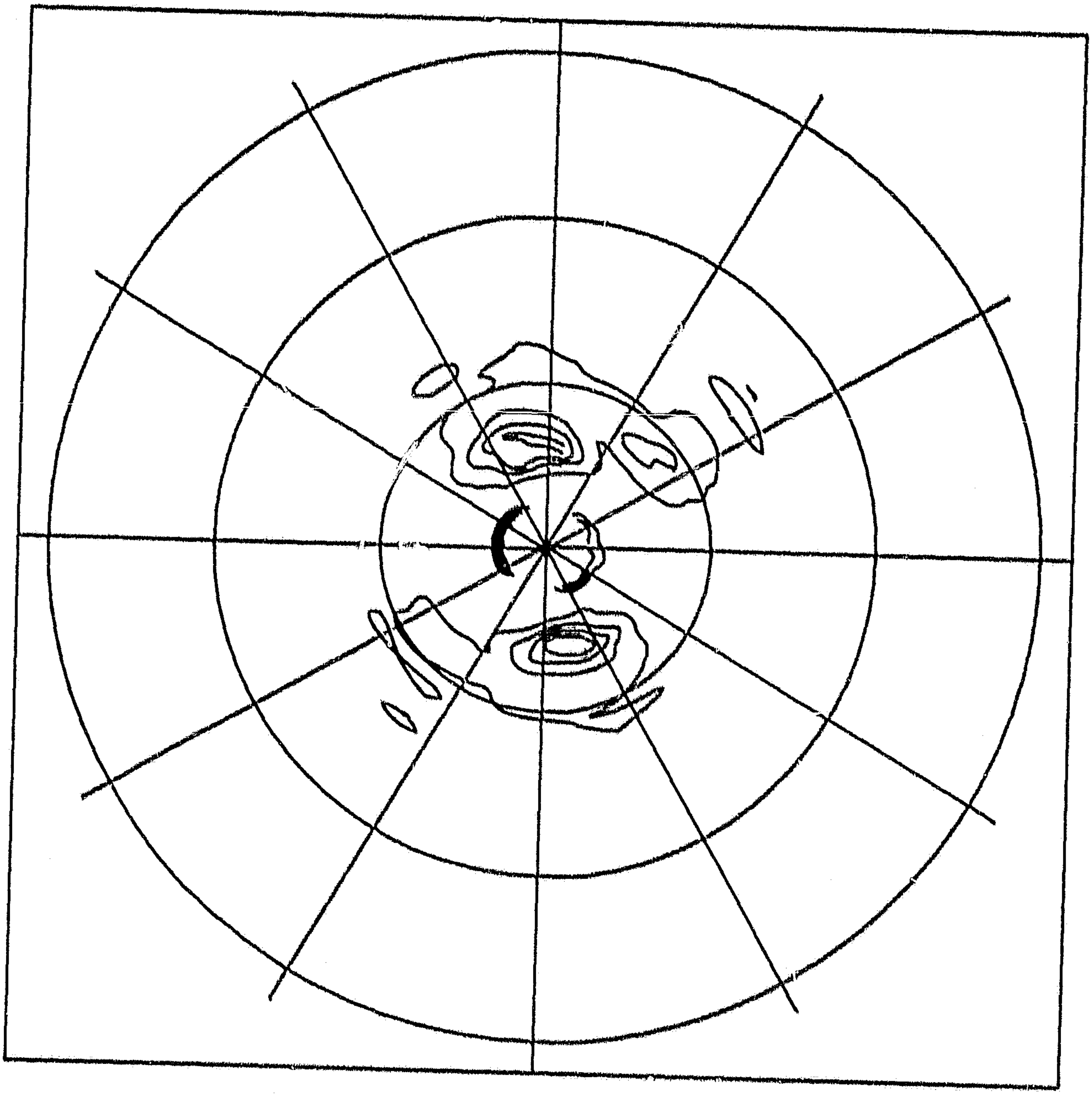

CLEV 4.3566 FRNG 0.30000E-02

FIGURE 8a

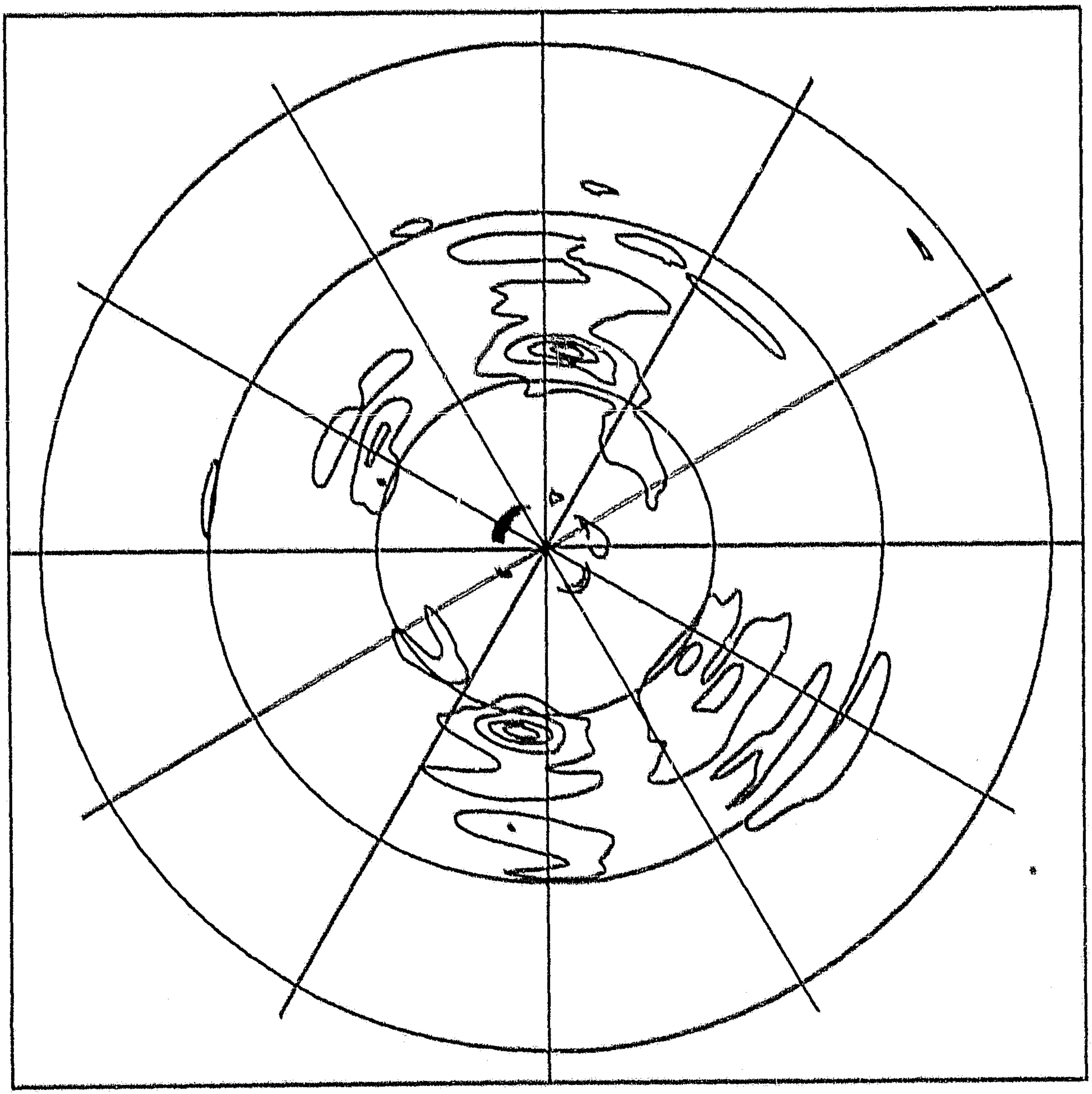

FLT-19 TAPE91 FILE-6 ROT

CLEV 2.5000 FRNG 0.50000E-02

FIGURE 8b

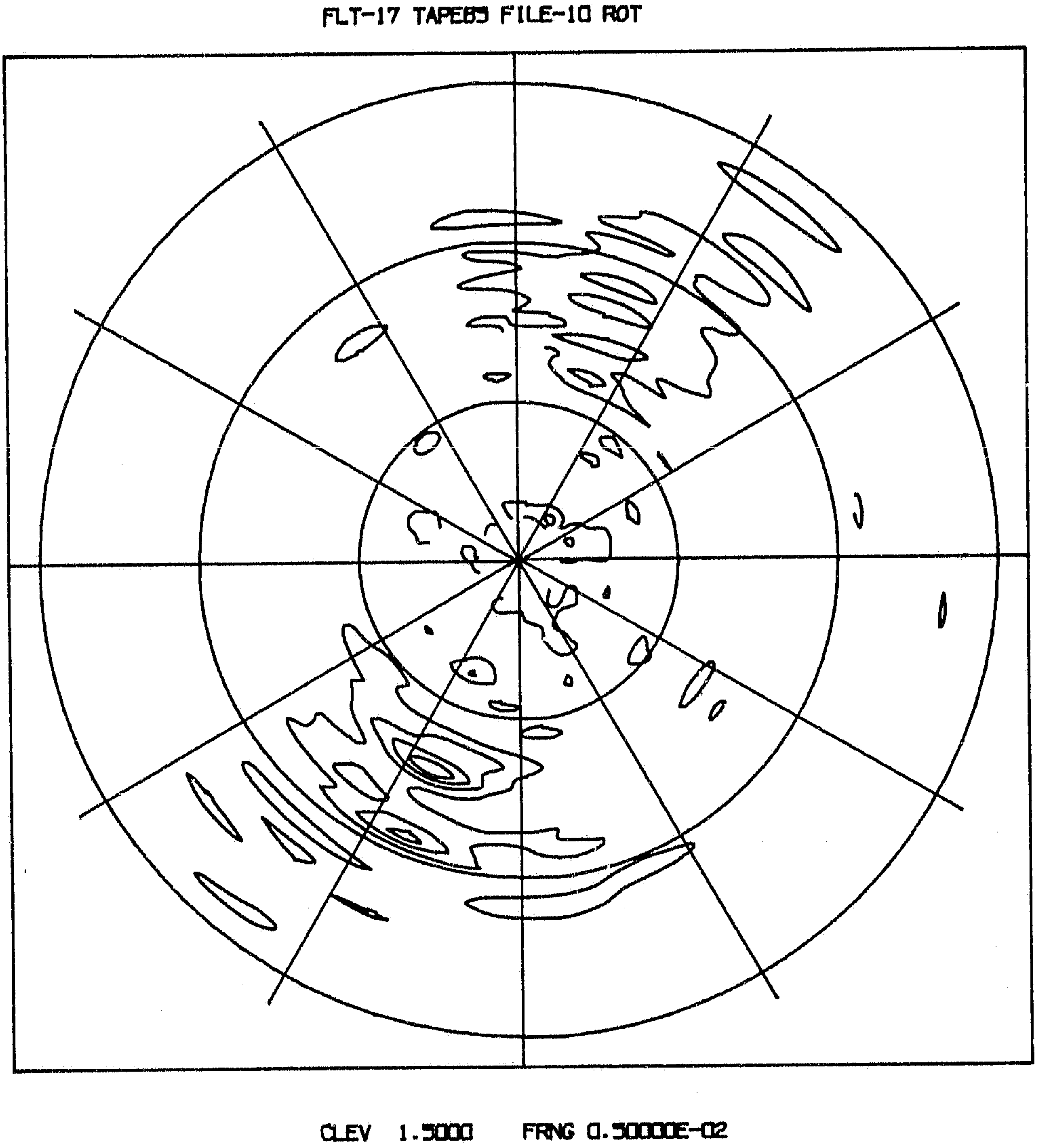

FIGURE 8c

ORIGINAL PAGE IS
OF POOR QUALITY

FLT-18 TAPE89 FILE-3 ROT

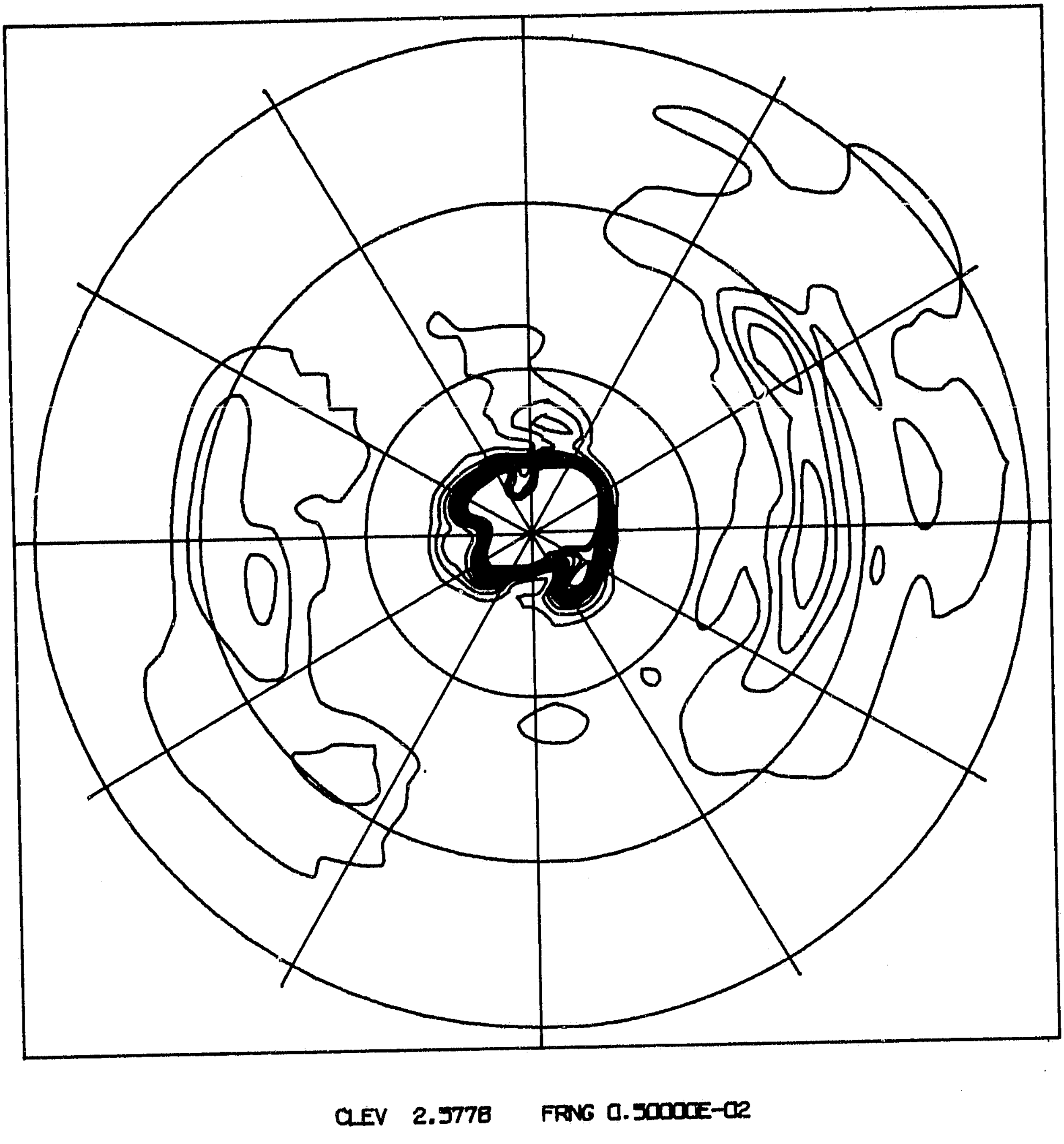

CLEV 2.3778 FRNG 0.50000E-02

FIGURE 8d

FLT-19 TAPE34 FILE-2 ROT

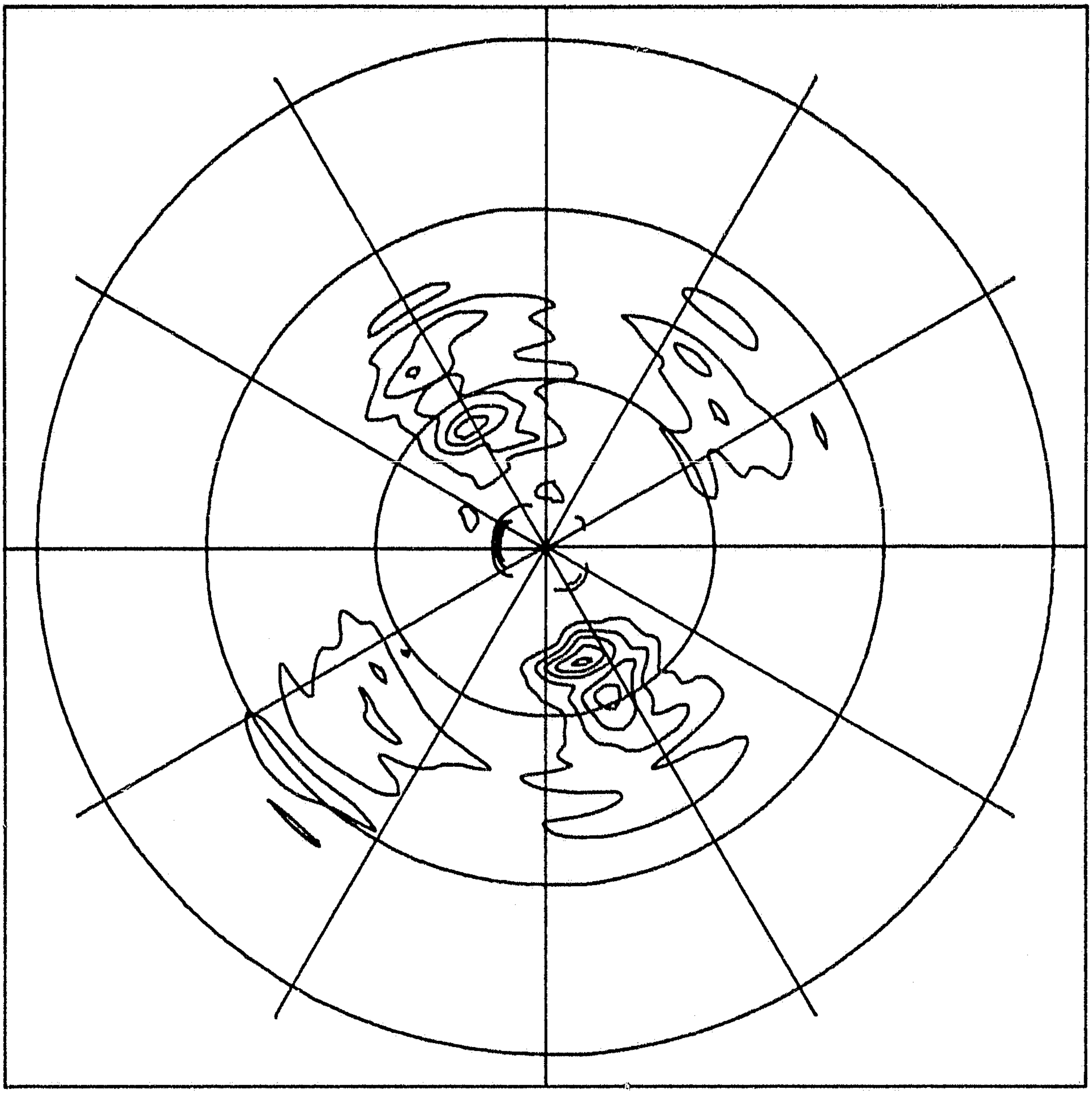

CLEV 1.8833 FRNG 0.50000E-02

FIGURE 8e

ORIGINAL PAGE IS
OF POOR QUALITY

FLT-18 TAPE90 FILE-7 ROT

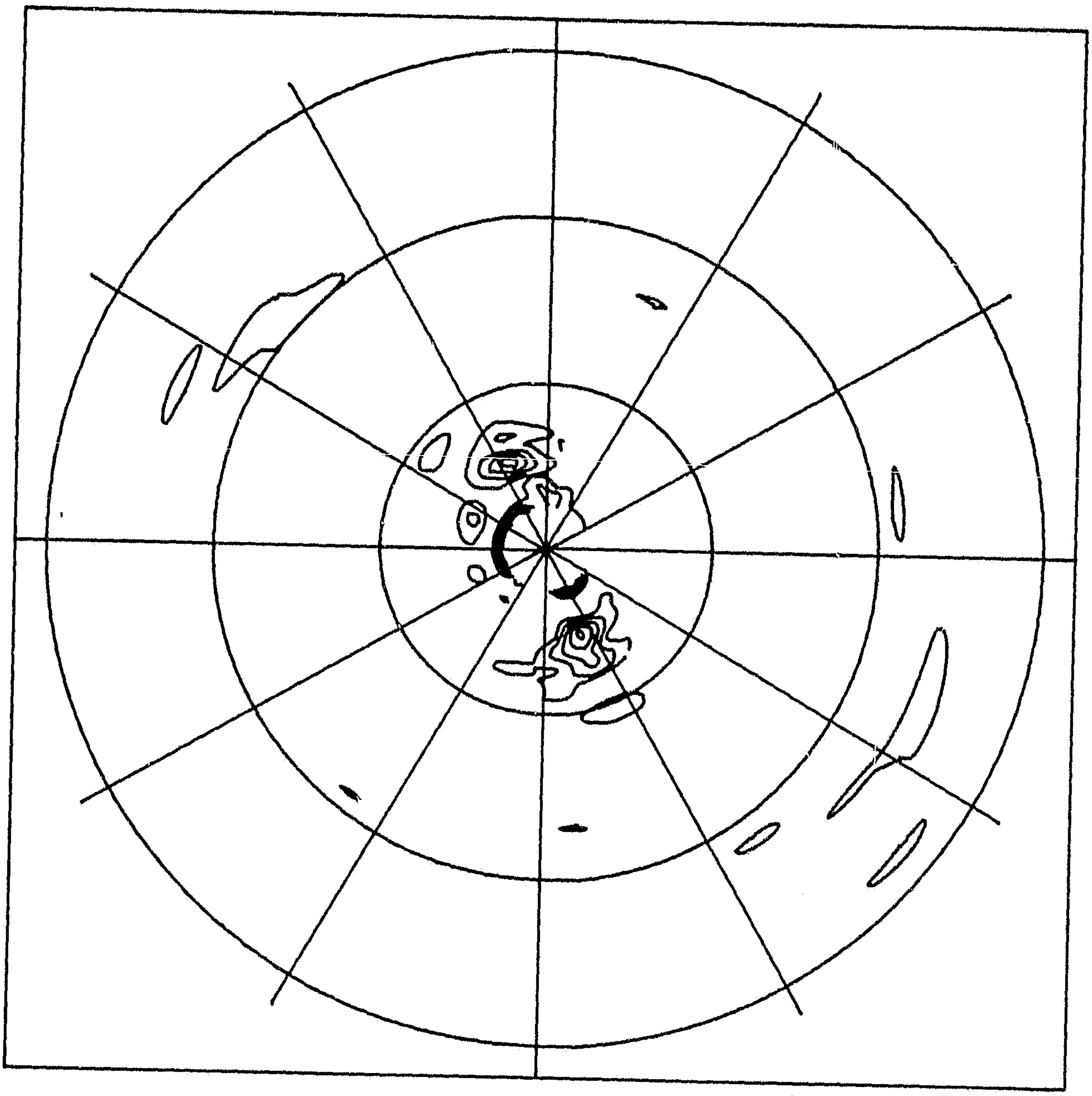

CLEV 1.4000 FRNG 0.50000E-02

FIGURE 8f

ORIGINAL PAGE IS
OF POOR QUALITY

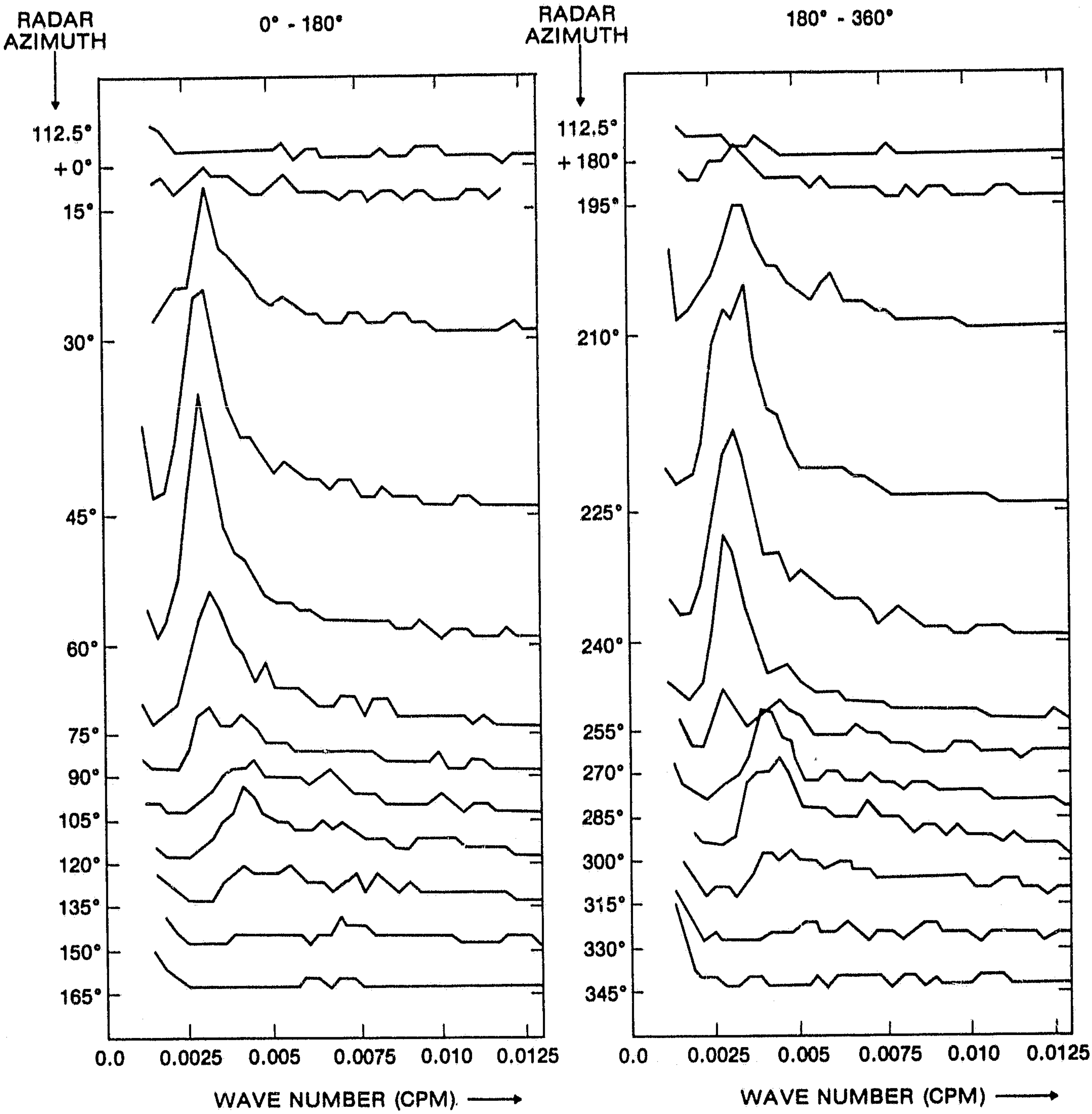

FIGURE 9

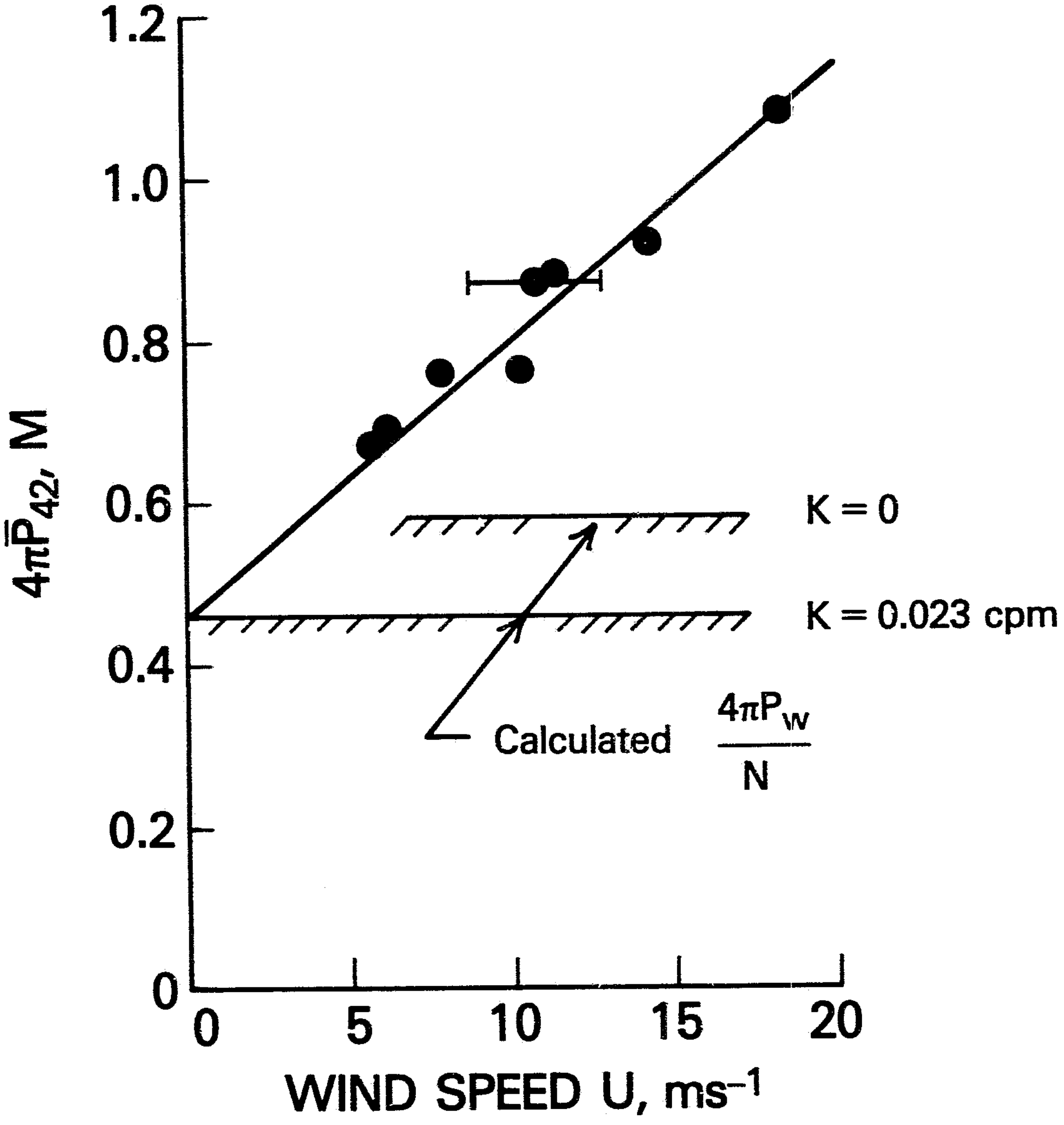
1.2
1.0
0.8
0.6
0.4
0.2
0
$4\pi\overline{P}_{42}$, M
K = 0
K = 0.023 cpm
Calculated $\frac{4\pi P_W}{N}$
0
5
10
15
20
WIND SPEED U, ms^{-1}

FIGURE 10

ORIGINAL PAGE IS
OF POOR QUALITY

FLT-9 TAPE367 FILE-1 ROT

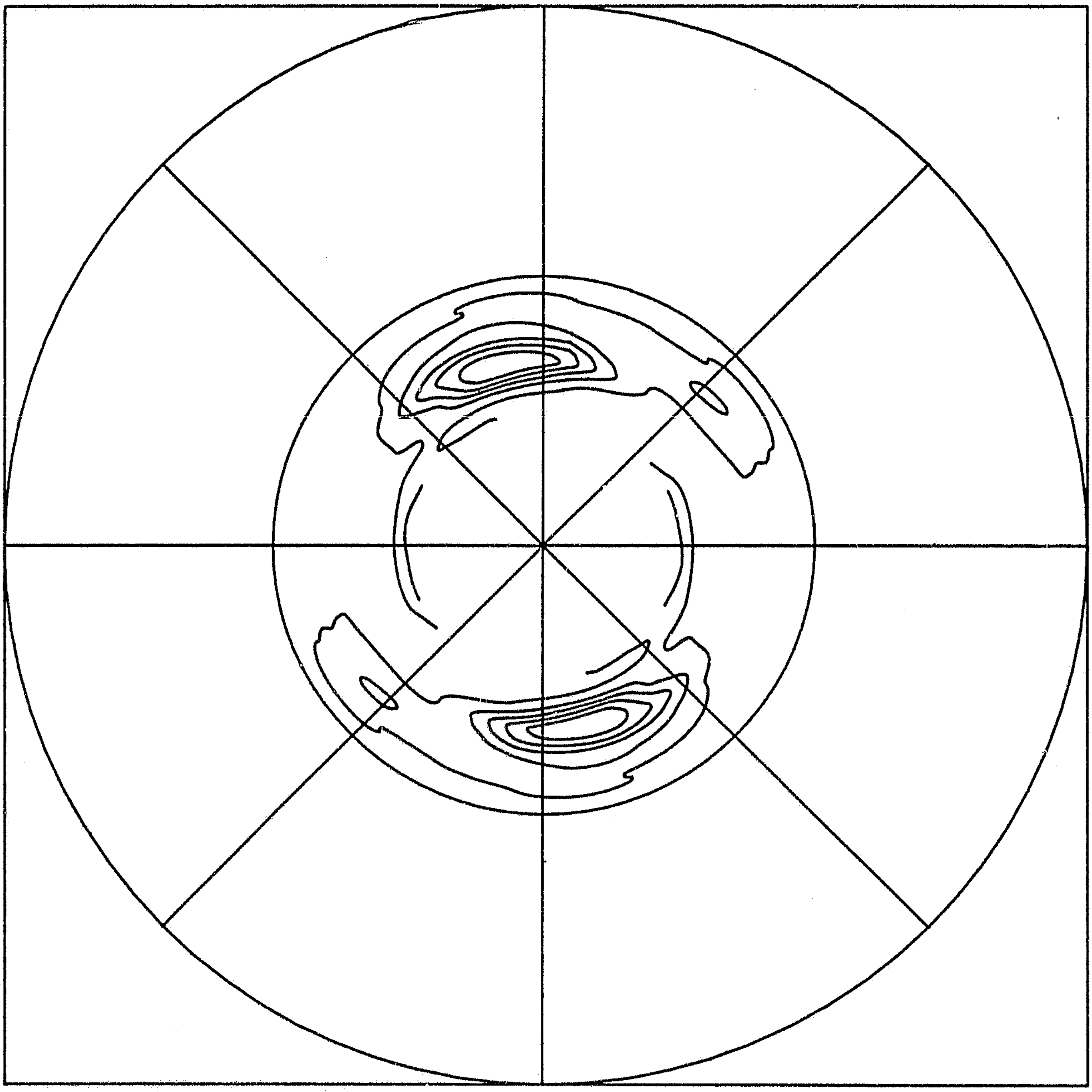

CLEV 69.999 FRNG 0.10000E 00

FIGURE 11a

ORIGINAL PAGE IS
OF POOR QUALITY

FLT-19 TAPE91 FILE-6 ROT

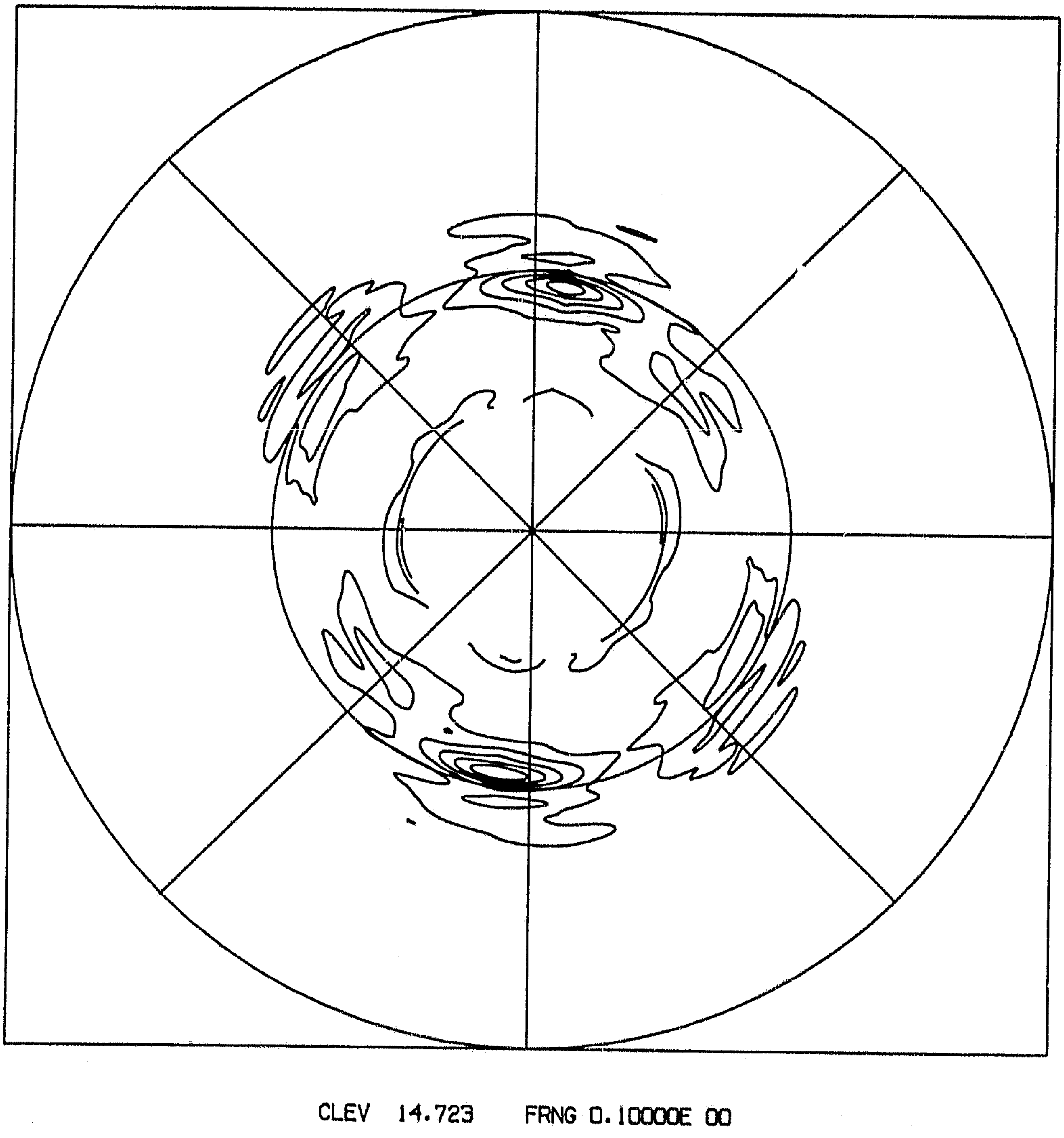

CLEV 14.723 FRNG 0.10000E 00

FIGURE 11b

ORIGINAL PAGE IS
OF POOR QUALITY

FLT-17 TAPE85 FILE-10 ROT

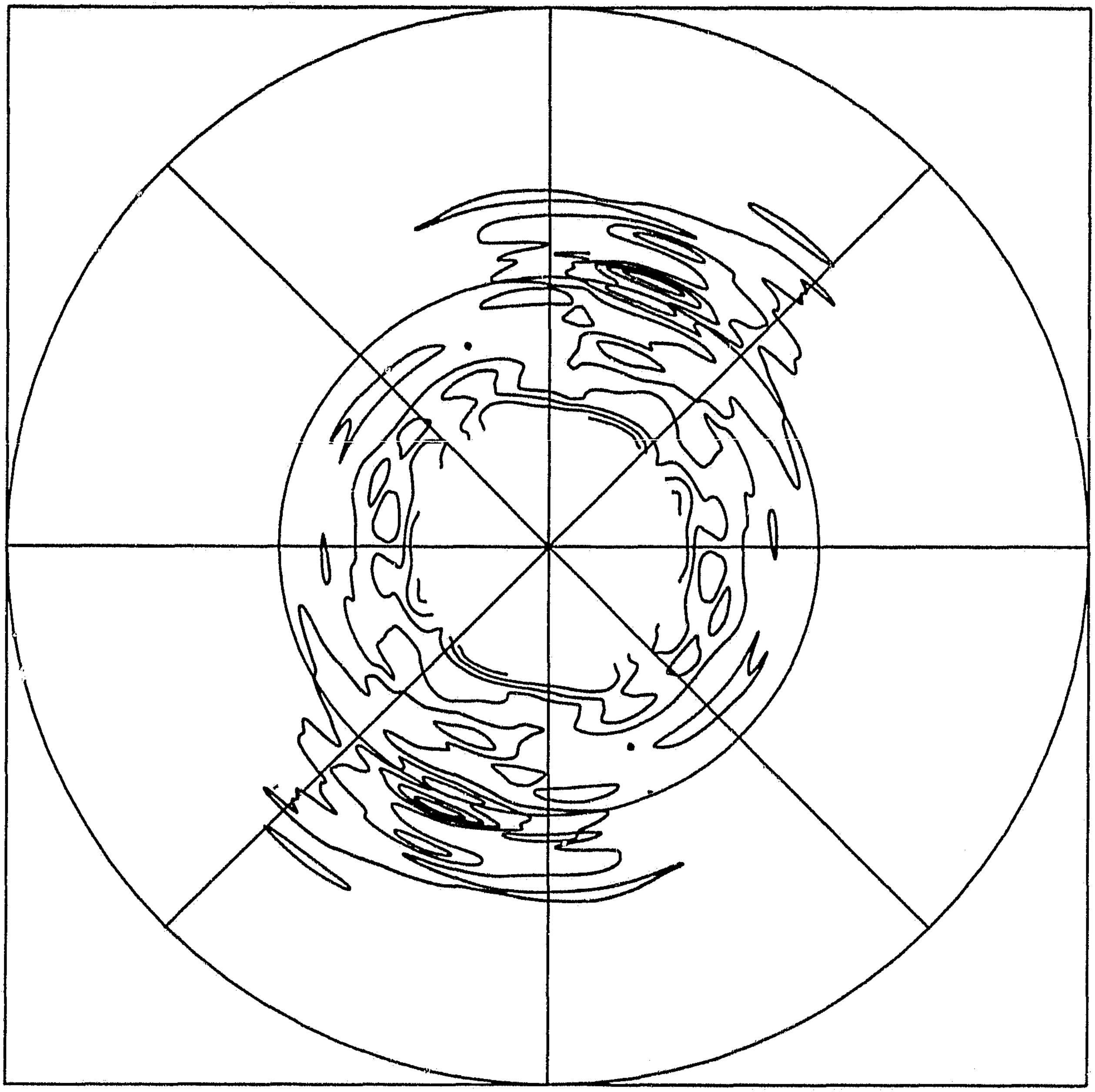

CLEV 4.6076 FRNG 0.10000E 00

FIGURE 11c

ORIGINAL PAGE IS
OF POOR QUALITY

FLT-18 TAPE89 FILE-3 ROT

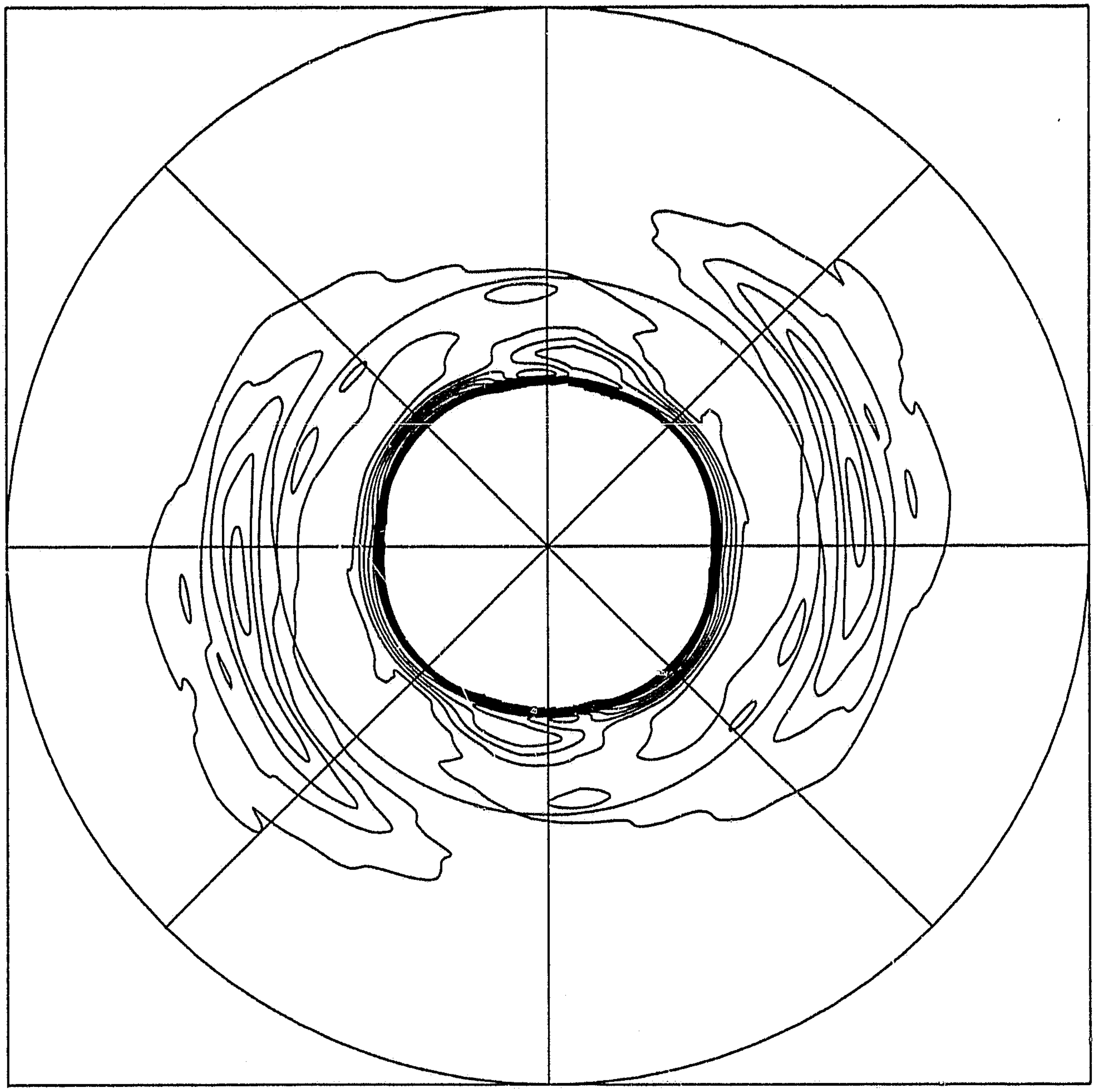

CLEV 5.7921 FRNG 0.10000E 00

FIGURE 11d

ORIGINAL PAGE IS
OF POOR QUALITY

FLT-19 TAPE94 FILE-2 ROT

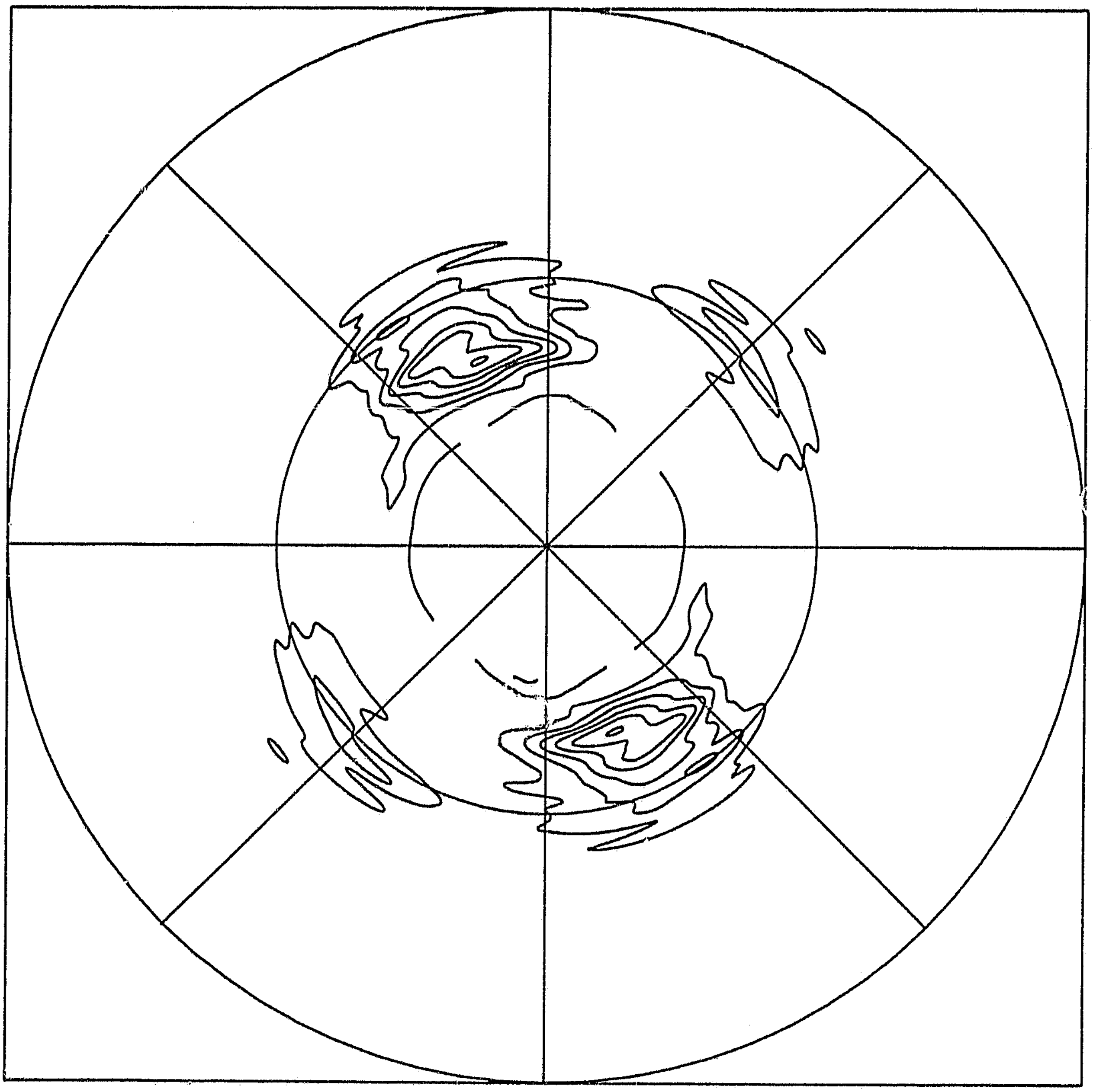

CLEV 11.360 FRNG 0.10000E 00

FIGURE 11e

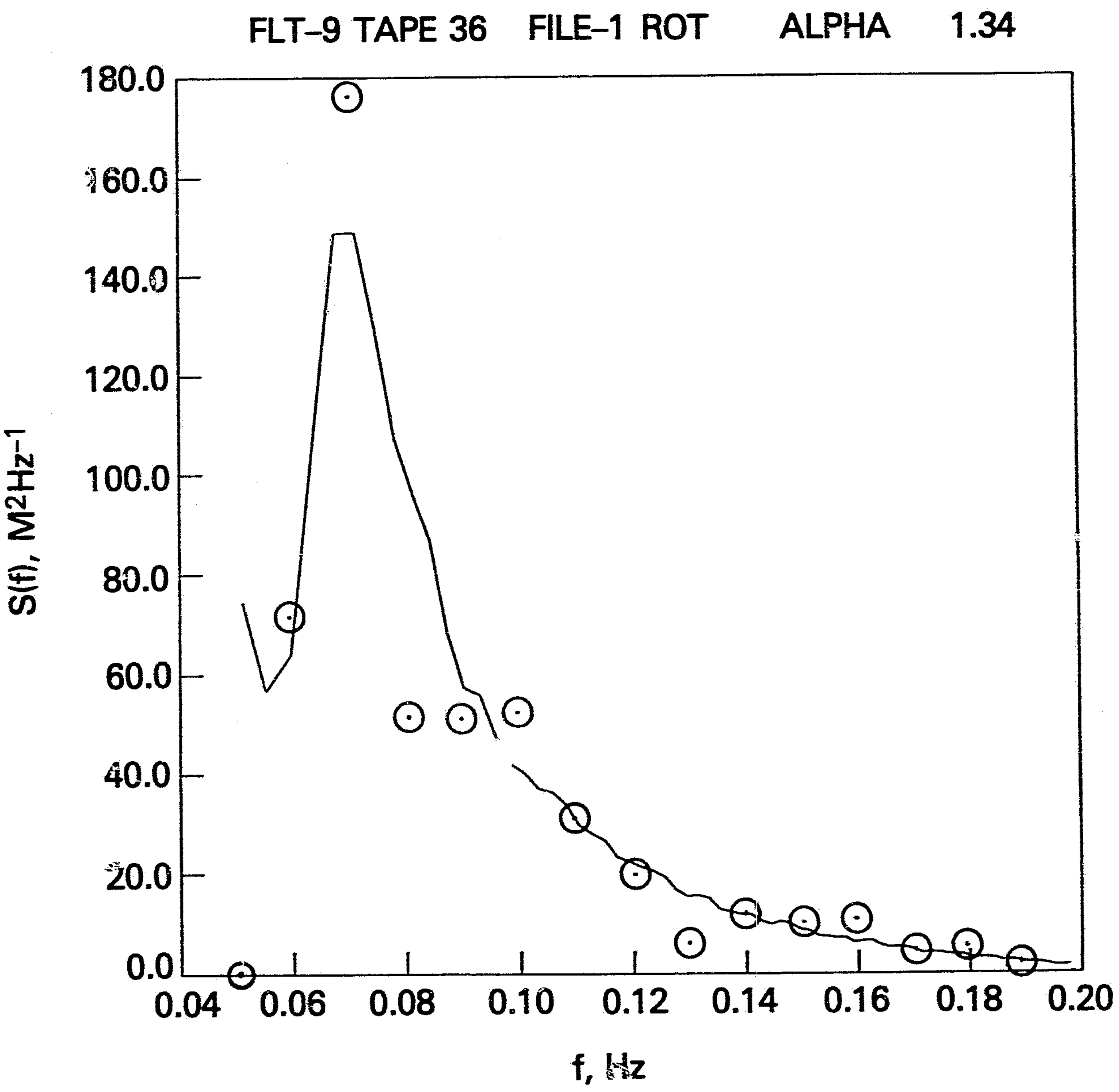
FLT-9 TAPE 36 FILE-1 ROT ALPHA 1.34
S(f), M²Hz⁻¹
180.0
160.0
140.0
120.0
100.0
80.0
60.0
40.0
20.0
0.0
0.04
0.06
0.08
0.10
0.12
0.14
0.16
0.18
0.20
f, Hz

FIGURE 12a

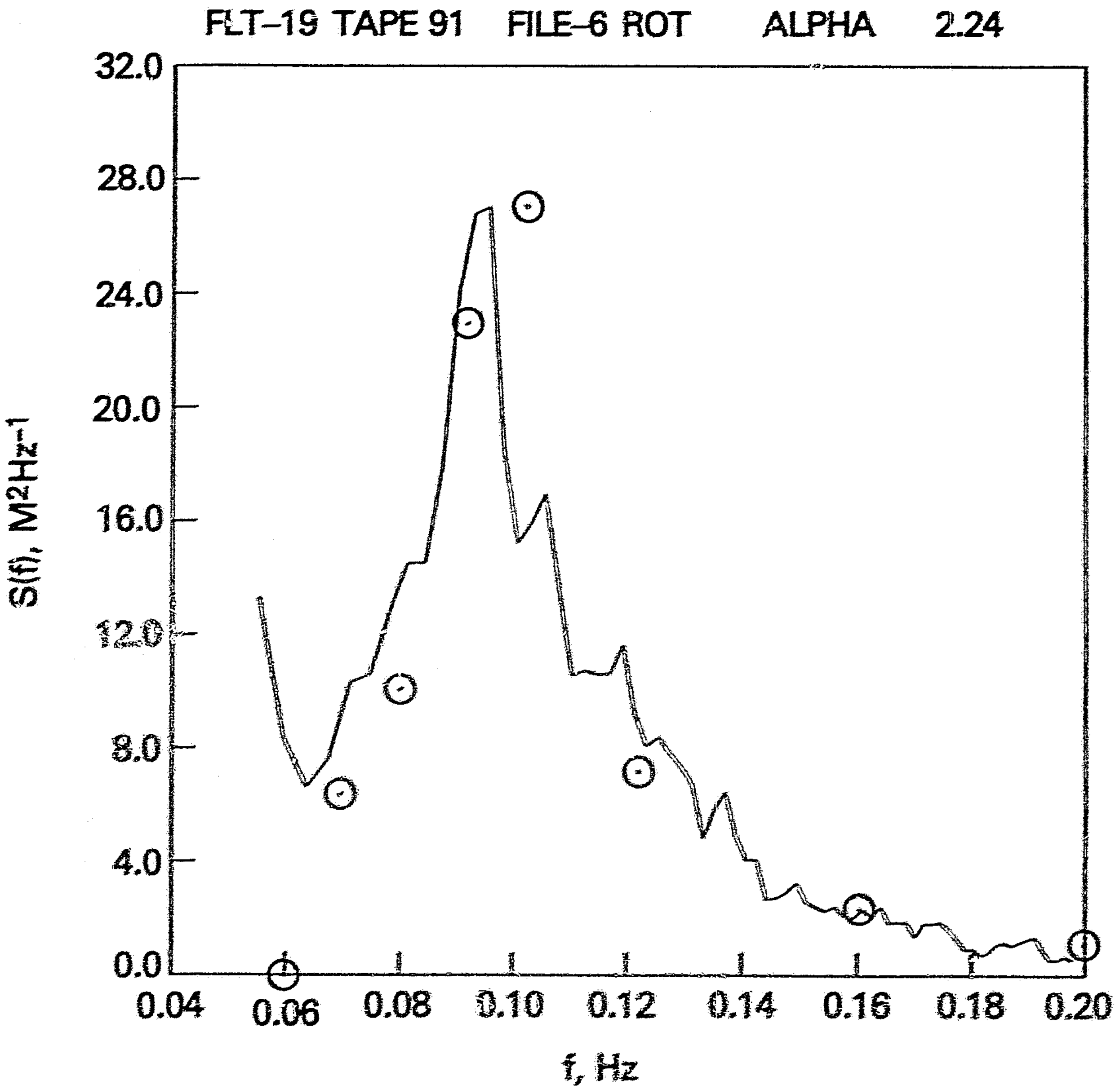
FLT-19 TAPE 91 FILE-6 ROT ALPHA 2.24
S(f), M²Hz⁻¹
32.0
28.0
24.0
20.0
16.0
12.0
8.0
4.0
0.0
0.04
0.06
0.08
0.10
0.12
0.14
0.16
0.18
0.20
f, Hz

FIGURE 12b

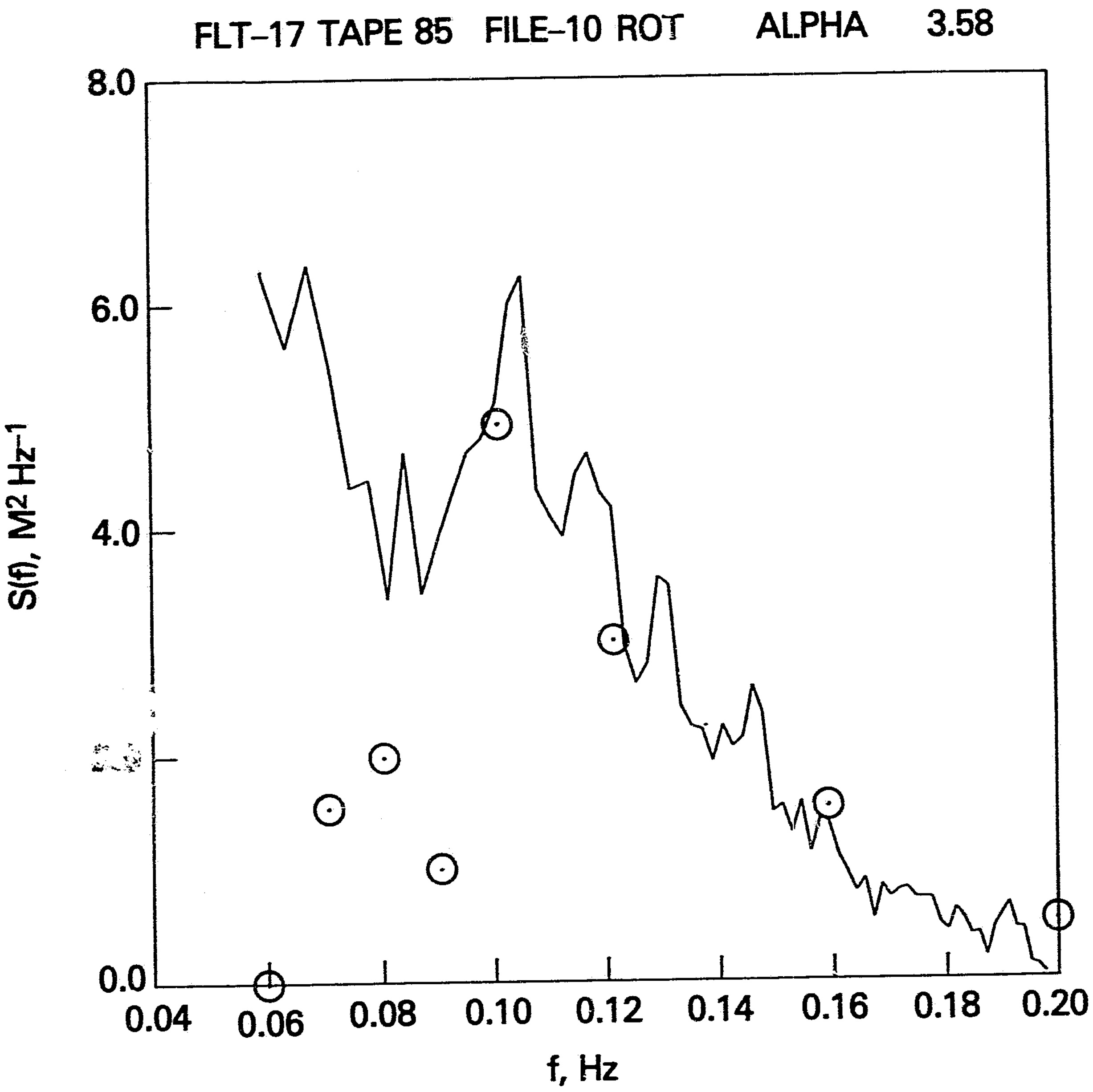
FLT-17 TAPE 85 FILE-10 ROT ALPHA 3.58
S(f), M² Hz⁻¹
8.0
6.0
4.0
2.0
0.0
0.04
0.06
0.08
0.10
0.12
0.14
0.16
0.18
0.20
f, Hz

FIGURE 12c

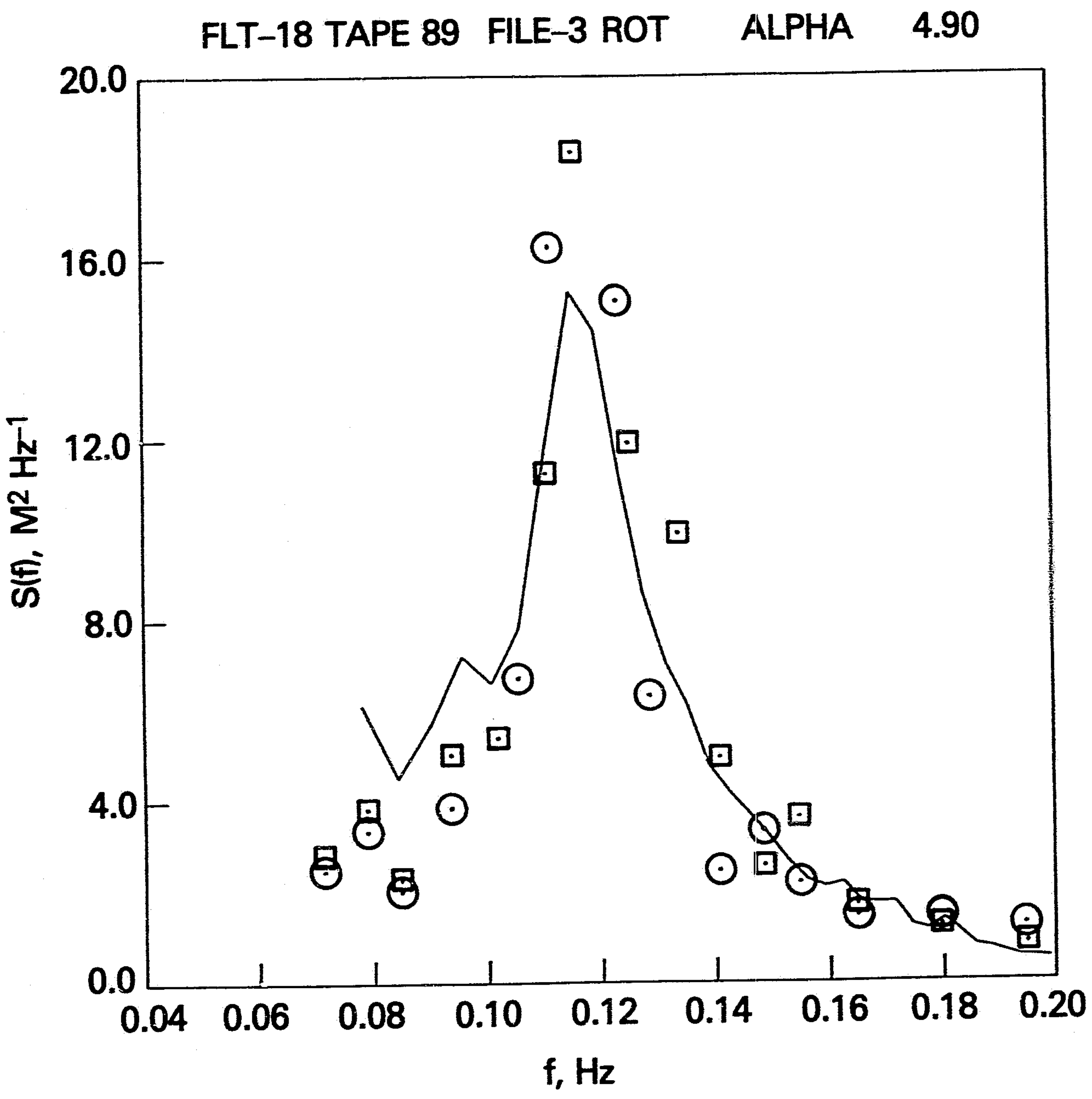
FLT-18 TAPE 89 FILE-3 ROT ALPHA 4.90
S(f), M² Hz⁻¹
20.0
16.0
12.0
8.0
4.0
0.0
0.04
0.06
0.08
0.10
0.12
0.14
0.16
0.18
0.20
f, Hz

FIGURE 12d

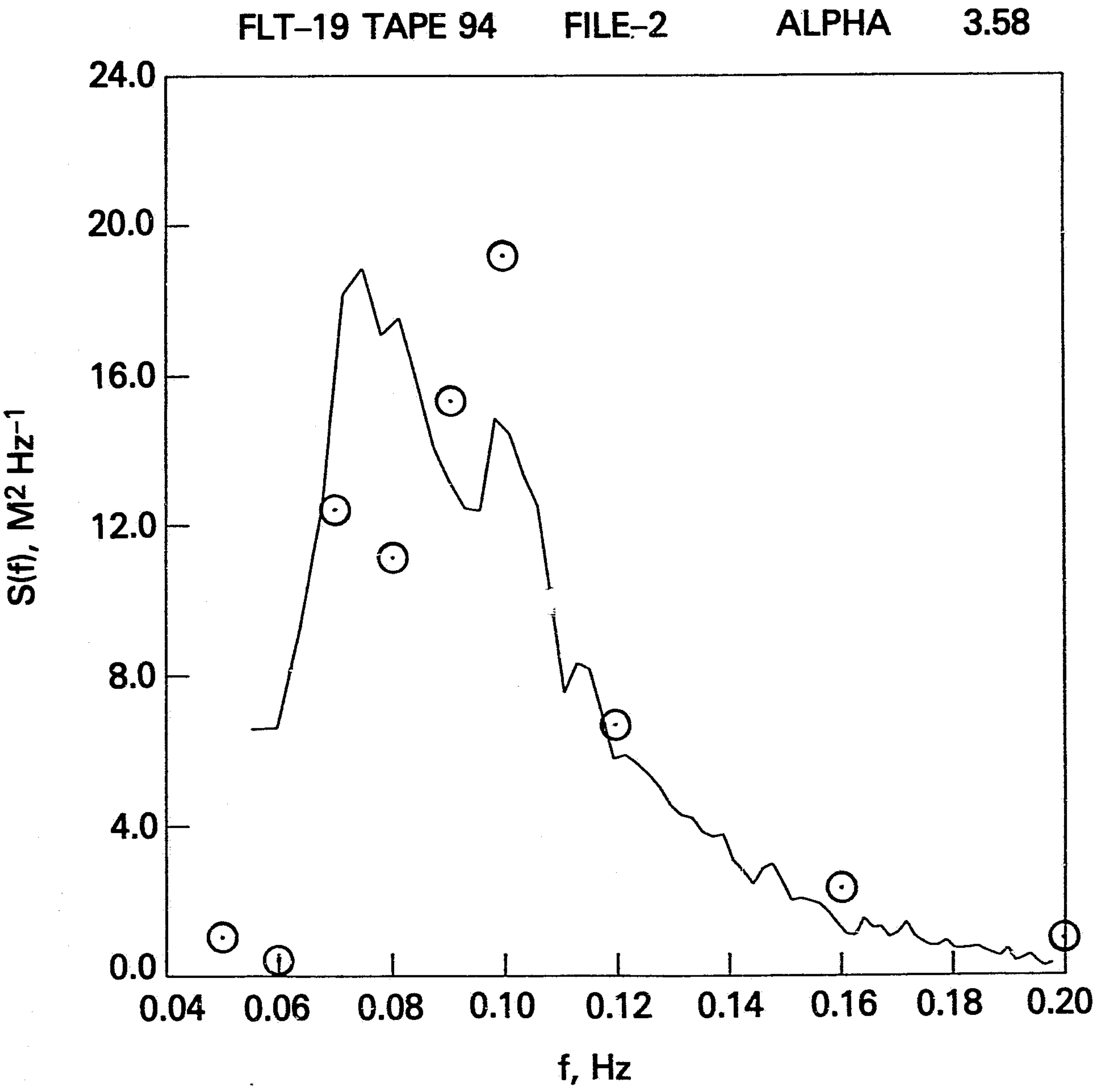
FLT–19 TAPE 94 FILE-2 ALPHA 3.58
S(f), M^2 Hz^{-1}
24.0
20.0
16.0
12.0
8.0
4.0
0.0
0.04
0.06
0.08
0.10
0.12
0.14
0.16
0.18
0.20
f, Hz

FIGURE 12e

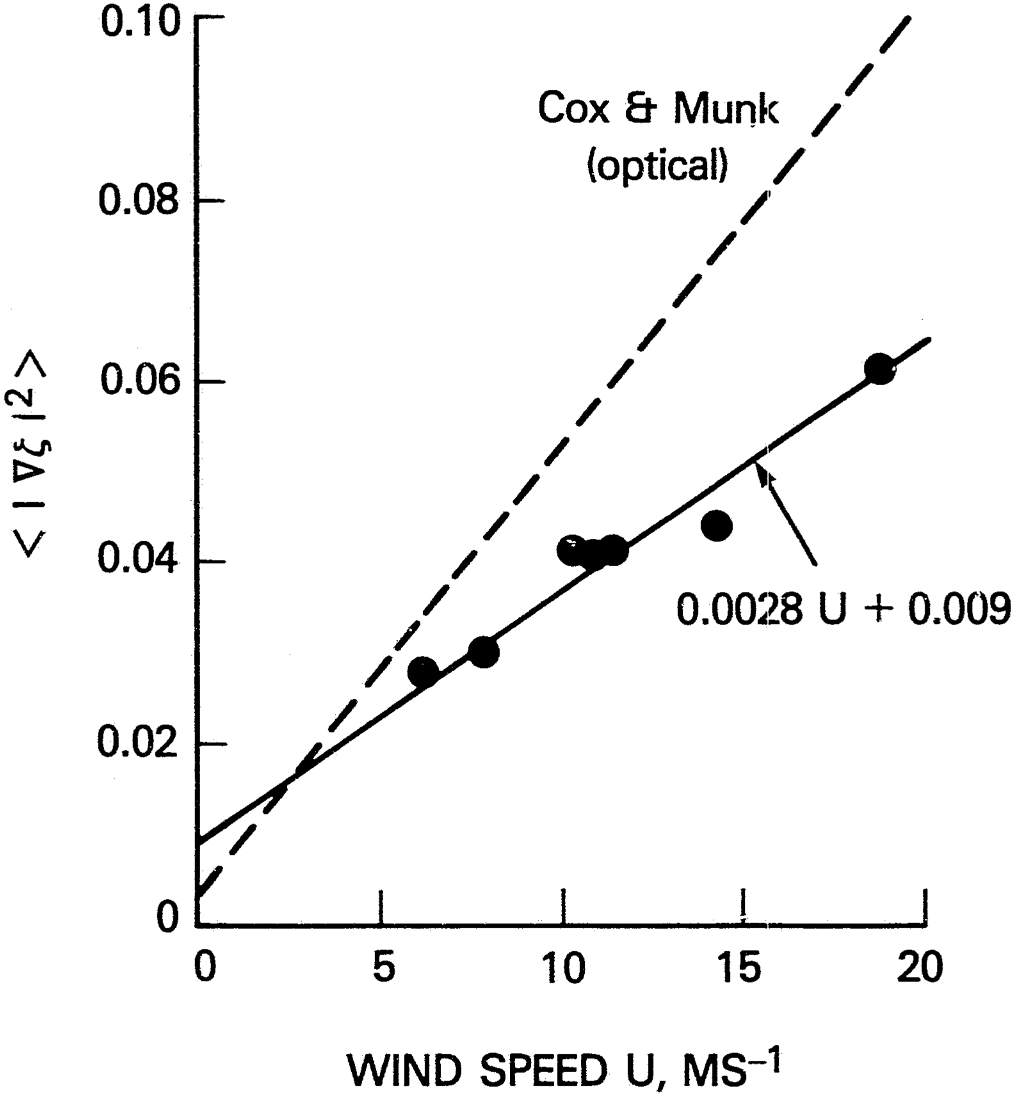

0.10
0.08
0.06
0.04
0.02
0
$< | \nabla\xi |^2 >$
Cox & Munk
(optical)
0.0028 U + 0.009
0
5
10
15
20
WIND SPEED U, MS^{-1}

FIGURE 13

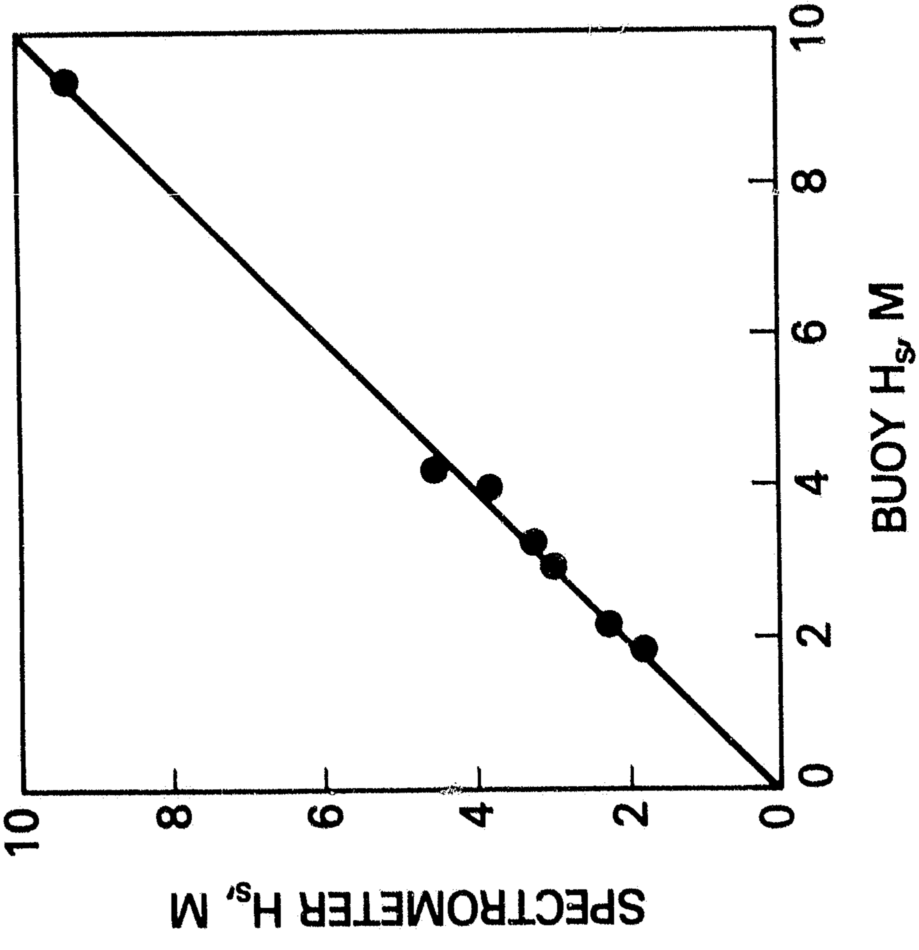

FIGURE 14

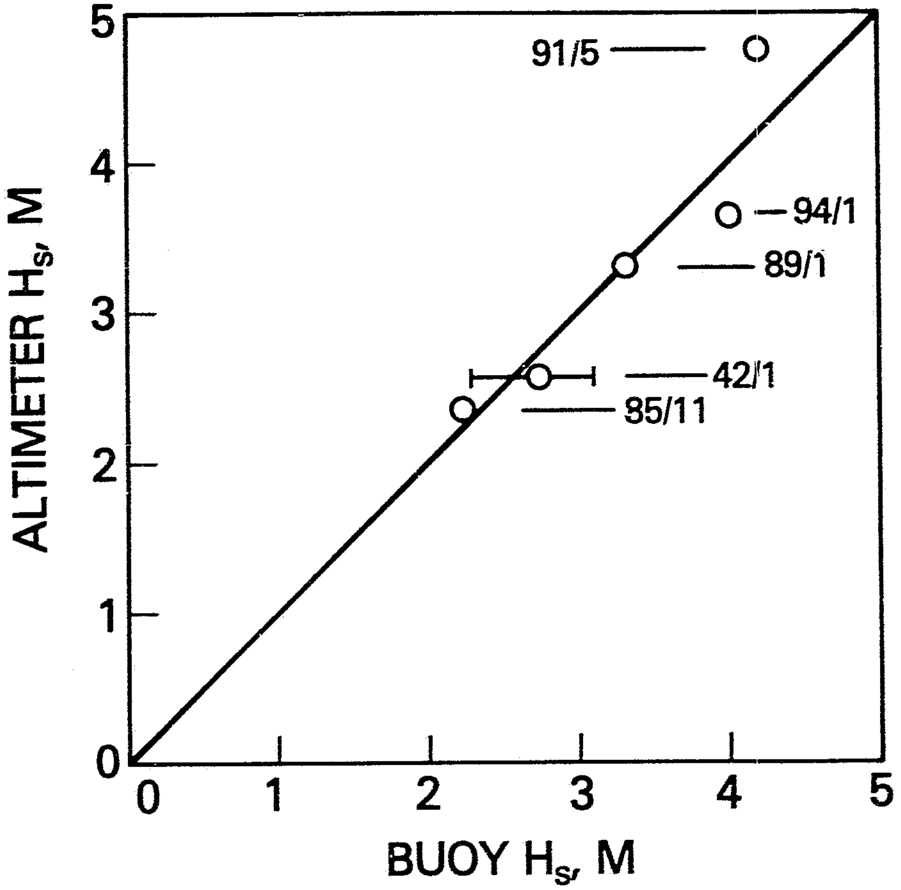

FIGURE 15

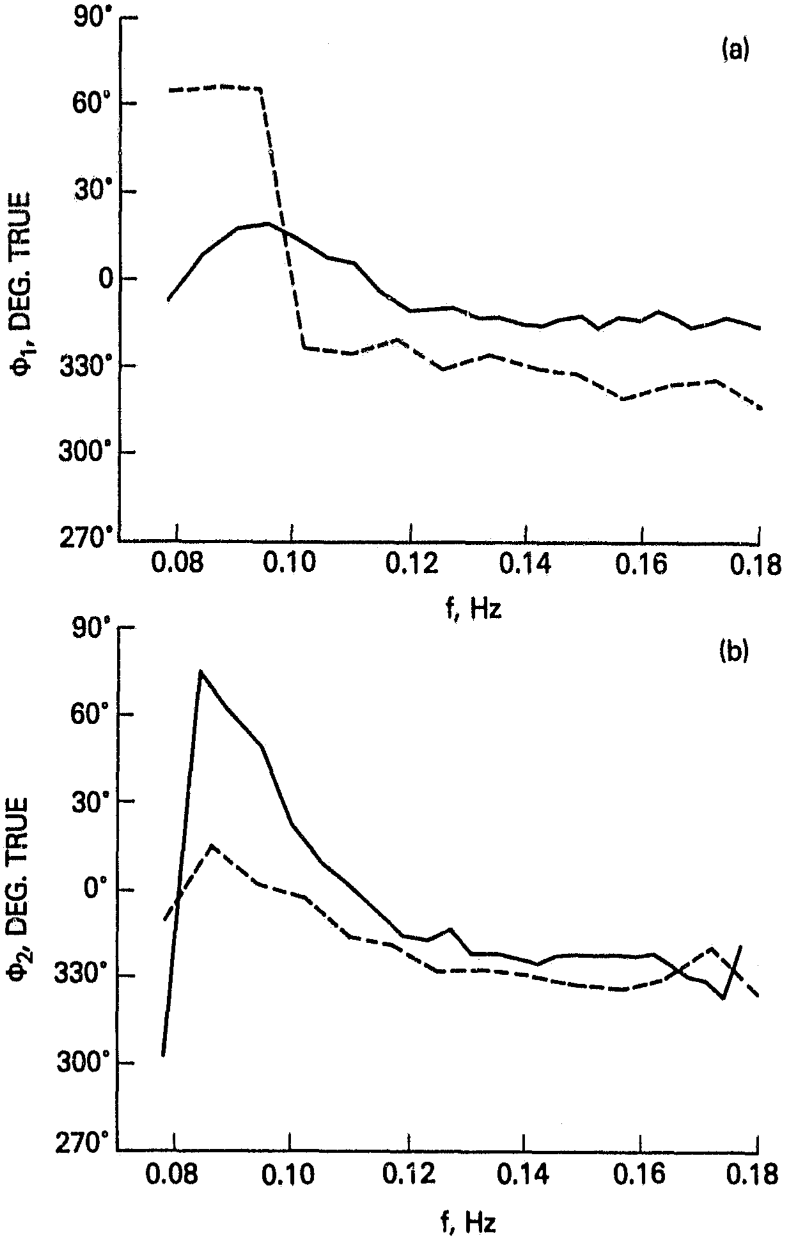
(a)
90°
60°
30°
0
330°
300°
270°
Φ1, DEG. TRUE
0.08
0.10
0.12
0.14
0.16
0.18
f, Hz
(b)
90°
60°
30°
0°
330°
300°
270°
Φ2, DEG. TRUE
0.08
0.10
0.12
0.14
0.16
0.18
f, Hz

FIGURE 16a,b

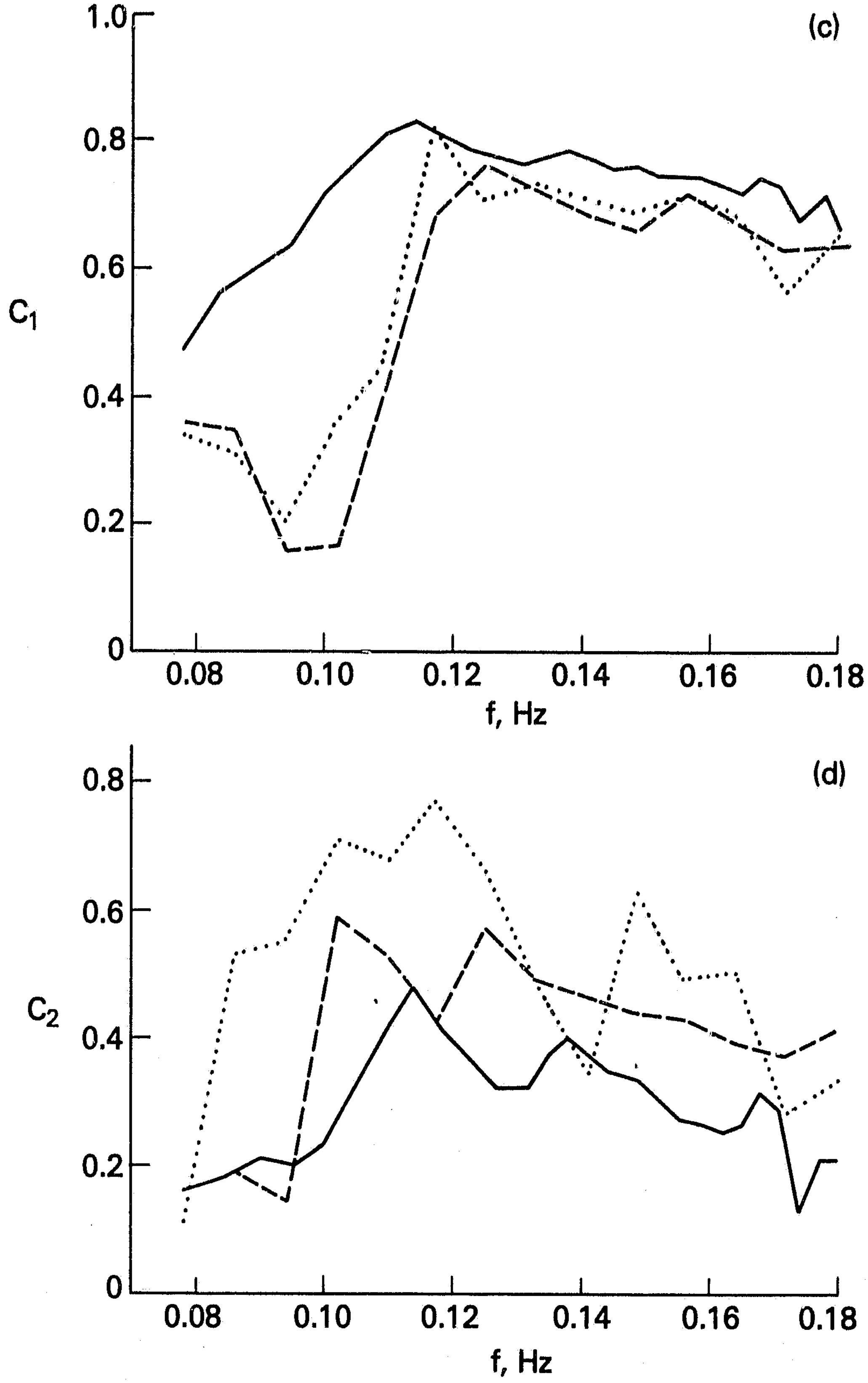
1.0
0.8
0.6
C1
0.4
0.2
0
(c)
0.08
0.10
0.12
0.14
0.16
0.18
f, Hz
0.8
0.6
C2
0.4
0.2
0
(d)
0.08
0.10
0.12
0.14
0.16
0.18
f, Hz

FIGURE 16c,d

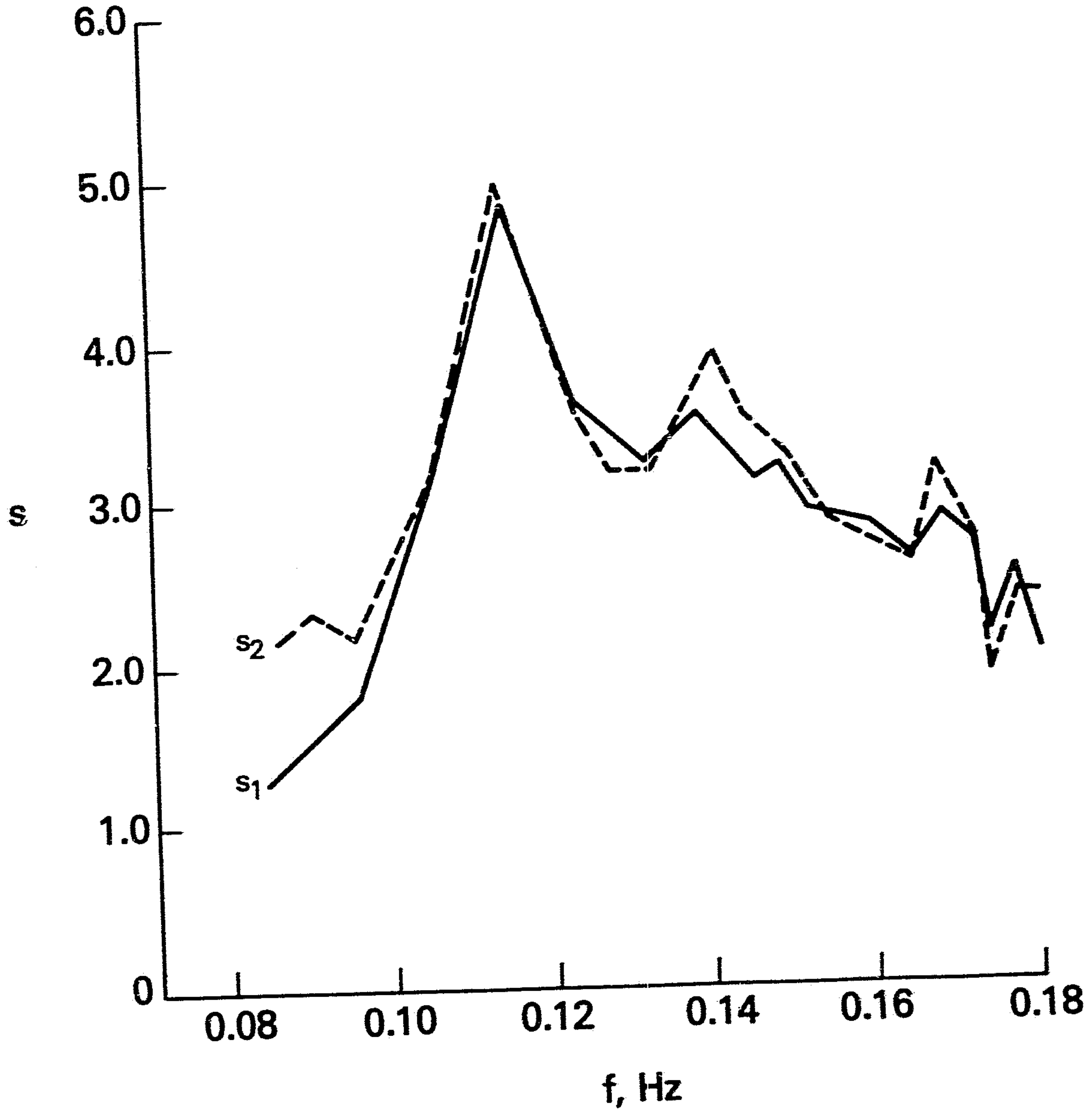

FIGURE 17

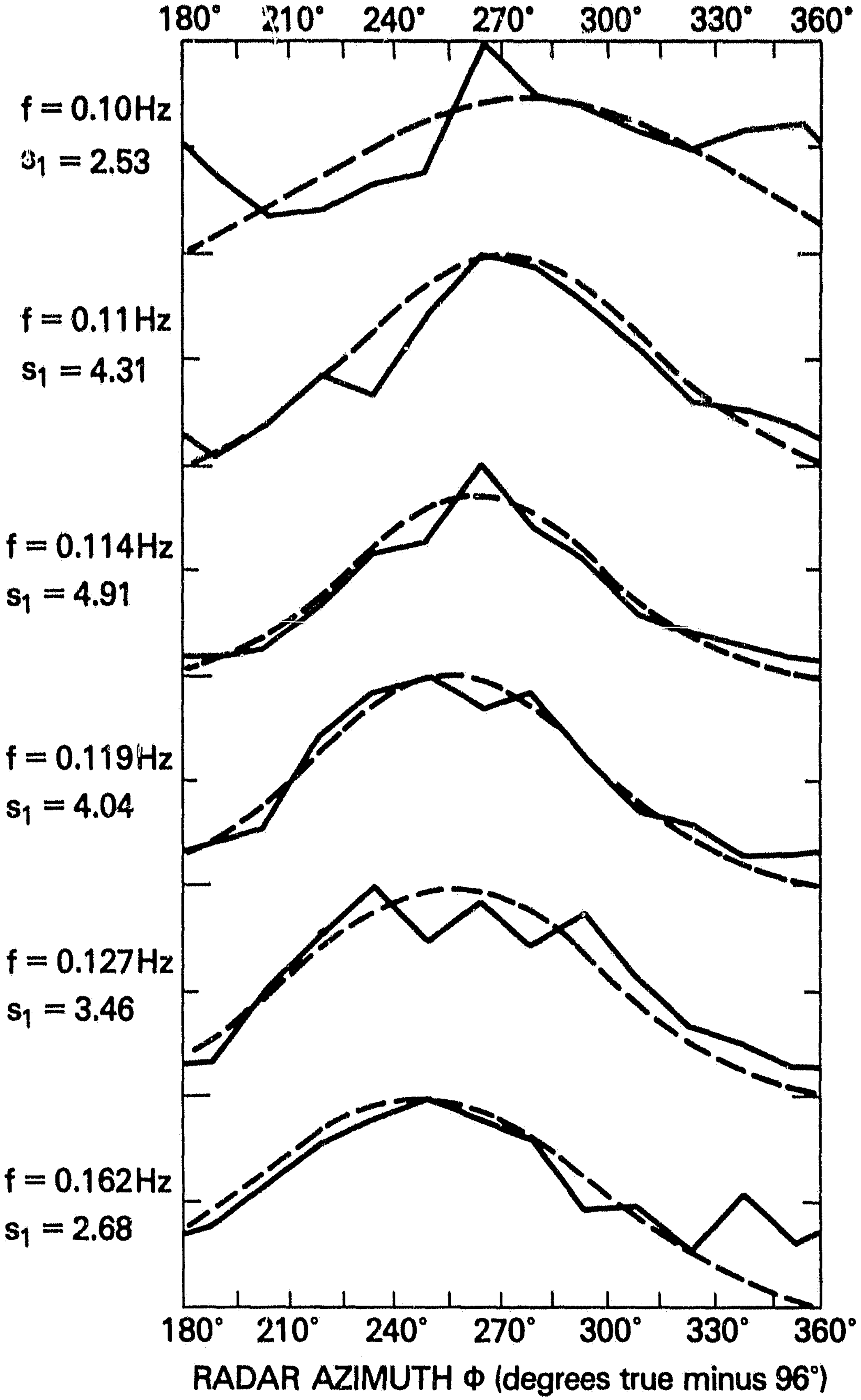

180°
210°
240°
270°
300°
330°
360°
f = 0.10Hz
s1 = 2.53
f = 0.11Hz
s1 = 4.31
f = 0.114Hz
s1 = 4.91
f = 0.119Hz
s1 = 4.04
f = 0.127Hz
s1 = 3.46
f = 0.162Hz
s1 = 2.68
RADAR AZIMUTH Φ (degrees true minus 96°)

FIGURE 18

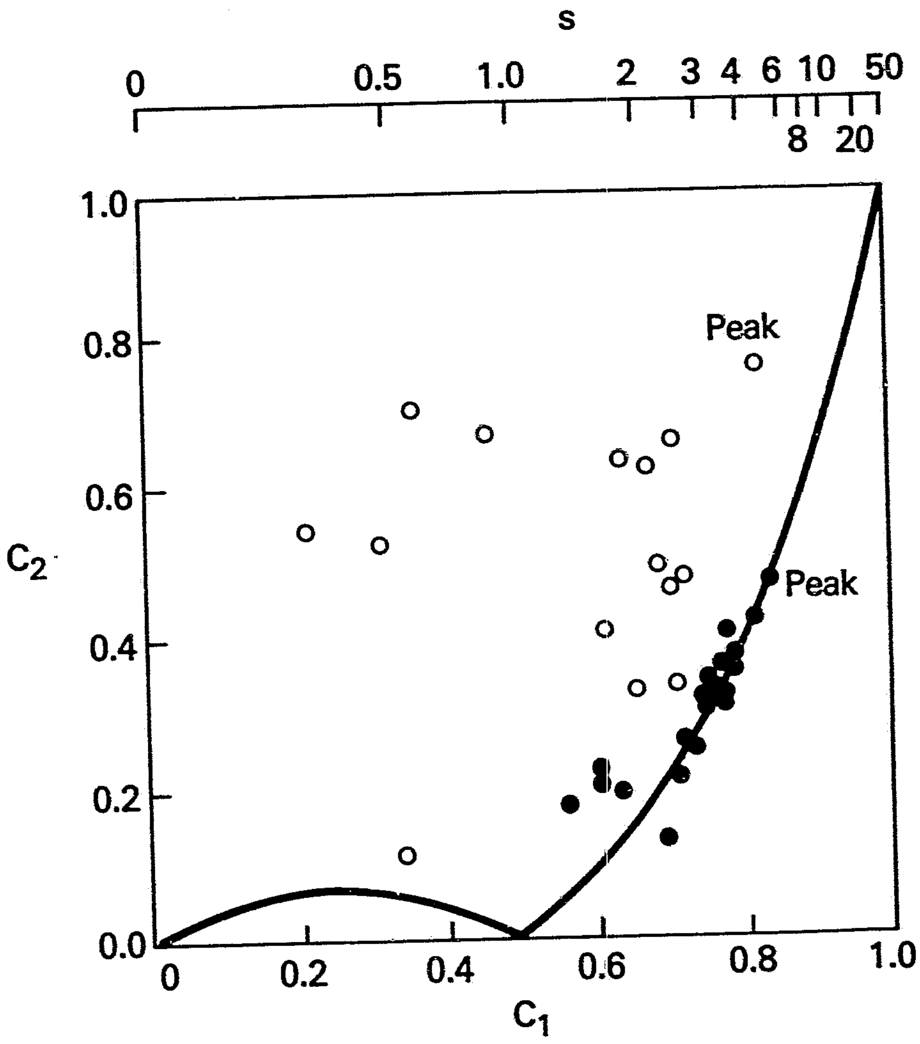
s
0
0.5
1.0
2
3
4
6
8
10
20
50
C_2
1.0
0.8
0.6
0.4
0.2
0.0
0
0.2
0.4
0.6
0.8
1.0
C_1
Peak
Peak

FIGURE 19